Shoemaker-Levy 9 and Plume-forming Collisions on Earth

MARK B.E. BOSLOUGH AND DAVID A. CRAWFORD

Department of Computational Physics and Mechanics
Sandia National Laboratories
Albuquerque, New Mexico 87185-0820

New York Academy
of Sciences

Shoemaker-Levy 9 and Plume-forming Collisions on Earth

MARK B.E. BOSLOUGH AND DAVID A. CRAWFORD

Department of Computational Physics and Mechanics
Sandia National Laboratories
Albuquerque, New Mexico 87185-0820

New York Academy
of Sciences

Shoemaker-Levy 9 and Plume-forming Collisions on Earth[a]

MARK B.E. BOSLOUGH AND DAVID A. CRAWFORD

Department of Computational Physics and Mechanics
Sandia National Laboratories
Albuquerque, New Mexico 87185-0820

ABSTRACT: Computational models for the July, 1994 collision of comet Shoemaker-Levy 9 with Jupiter have provided a framework for interpreting the observational data. Imaging, photometry, and spectroscopy data from ground-based, Hubble Space Telescope, and Galileo spacecraft instruments are consistent with phenomena that were dominated by the generation of incandescent fireballs that were ballistically ejected to high altitudes, where they formed plumes that subsequently collapsed over large areas of Jupiter's atmosphere. Applications of similar computational models to collisions into Earth's atmosphere show that a very similar sequence of events should take place for NEO impacts with energies as low as 3 megatons, recurring on 100 year timescales or less. This result suggests that the 1908 Tunguska event was a plume-forming atmospheric explosion, and that some of the phenomena associated with it might be related to the ejection and collapse of a high plume. Hazards associated with plume growth and collapse should be included in the evaluation of the impact threat to Earth, and opportunities should be sought for observational validation of atmospheric impact models by exploiting data already being collected from the natural flux of multikiloton to megaton sized objects that constantly enter Earth's atmosphere on annual to decadal timescales.

INTRODUCTION

When pieces of the broken comet Shoemaker-Levy 9 slammed one-by-one into Jupiter in 1994, the overall physical consequences were out of proportion with even the most enthusiastic predictions. The fallout included a transformation of public perceptions about the impact threat to Earth, because the reality of planetary collisions no longer could be dismissed. Commentators described the event as a wake-up call, and it led some policy makers — for the first time — to take seriously the hazards from comets and asteroids. Some members of the scientific community also changed their opinions because the visible consequences of the collision were so much greater than anticipated. Proponents of detection and mitigation pursuits are now able to point to the impact on Jupiter when they make the case for an

236

increase in effort directed at discovering near-Earth objects, or for developing a means to protect our planet from them.

By contrast, the main scientific lesson learned from the devastation on Jupiter was not that large, fast objects collide with planets. That fact had been established decades earlier by analyzing the cratered planetary surfaces, and its importance had been brought home by more recent research into the geologic record of Earth's craters, impact catastrophes, and mass extinction of life. For scientists, the principal revelation from the crash of SL-9 was that the direct aftermath — especially the complex sequence of phenomena that followed — far exceeded our capability to predict. Fortunately, no lives depended on any decisions that were based on the preimpact predictions of the Jovian catastrophe. If the demise of this comet is to be taken as a warning, it should be that even the most sophisticated modeling and theoretical studies, by themselves, do not yield a framework of knowledge that is sufficiently reliable for making major policy decisions. Conversely, the data from observed impacts such as these, by themselves, cannot be fully interpreted and understood without the framework that can be provided by computational models. Models and simulations of phenomena that take place over many orders of magnitude in time, distance, and energy scales need to be checked against actual data. In the case of collisions into planetary atmospheres, we now have been able to take advantage of a validation "experiment" in the form of a rare impact on another planet.

Even though SL-9 provides the only real benchmark data for large-scale hypervelocity collisions with atmospheres, our understanding of such events will continue to improve along with our modeling capabilities. It is humbling to note that — even when extensive data are available — there can still be a wide variation in interpretations and quantitative assessments. Postimpact estimates of mass (or energy) have varied by several orders of magnitude among modelers who are considering the same set of astronomical imagery and lightcurve data. As the models begin to converge, the best estimates still vary over a wide range. This observation naturally leads one to question the quantitative accuracy of estimates of the consequences for our own planet of an impact of a given size. An obvious response would be that the observable phenomena that resulted from the impact on Jupiter are not the same type of phenomena that would kill people and cause property damage on Earth. For example, a Tunguska-scale impact on Earth might be a plume-forming, lightcurve-generating event, but the threat to surface-dwellers would be from the blast wave, which is easier to relate to the yield. Nevertheless, the impact of SL-9 underscores the fact that the most important effects resulting from a complex sequence triggered by a single event are not always those that are anticipated.

For this reason, we have begun to take a closer look at the Tunguska event by applying what we have learned from SL-9. The Tunguska explosion has

also been attributed to an impactor with an estimated mass and yield that var-
ies by several orders of magnitude. The most commonly quoted magnitude
of the explosion (about 12 megatons) is still not universally accepted, and
many researchers have argued for a larger or smaller value. By applying the
simulation methods we used for SL-9, we are beginning to develop more in-
sight into the energy deposition into the atmosphere at Tunguska. We have
found that Tunguska is very much a terrestrial analogue of the SL-9 impact.
It was entirely an atmospheric event, in which the Earth's surface played
very little role other than acting as a "witness plate," covered with trees that
would be knocked down and charred for later examination. Because atmo-
spheric entry physics is similar on Earth, the Tunguska event probably gen-
erated a plume very similar to those that were seen on Jupiter. This paper
reviews the impact of SL-9, interprets it in the context of the computational
models, and presents Tunguska as a terrestrial example of the same process.

SHOEMAKER-LEVY 9

The multiple impacts on Jupiter in July 1994 provided a remarkable first
opportunity to observe the immediate results of a hypervelocity collision be-
tween a comet and a planet. Astronomers and modelers have analyzed in detail
the collision phenomena and aftermath, leading to advances in our understand-
ing of comets, of Jupiter, and of the collisional processes that shaped the solar
system. We are now beginning to take advantage of this improved understand-
ing to develop better models for the assessment of the impact threat to Earth.
The SL-9 impacts provided a free "natural experiment" that we could ex-
ploit to validate computational simulations (involving velocities, masses,
and kinetic energies many orders of magnitude higher than had ever before
been witnessed), using the shock physics codes (CTH and PCTH) that had
been developed at Sandia National Laboratories [27]. Traditionally, experi-
ments or scaled tests are used to provide data to check the validity of a com-
plex computational simulation against the real world. The natural
astronomical event allowed us to use observational data for validating our
simulations. As a spin-off, we were able to provide predictions to help guide
astronomical observations of the event. These predictions led to our primary
preimpact recommendation to observational astronomers: that the most use-
ful Earth-based measurements to be made within a few minutes after impact
would be time-resolved photometry at the Jovian limb [3]. More recently, we
have used our models and simulations to assist astronomers and planetary
scientists in interpreting the observational data.
Prior to impact, the computational effort was focused primarily on making
predictions. In the period between the recognition in mid-1993 that SL-9
would strike Jupiter, and the availability of new astrometric data after Jupiter
emerged from solar conjunction at the end of that year, the estimated point of

impact was far on Jupiter's back side (the history of the preimpact orbital calculations is reviewed by Chodas and Yeomans[11]). There was little hope for a direct view from Earth, and many astronomers were resigned to the very limited possibilities of observing reflections from Jupiter's inner satellites, or of seeing residual atmospheric disturbances that would rotate into view several hours after impact. After the better orbital data revealed that the impact point for some of the brightest fragments would be less than six degrees over the Jovian limb, various modeling groups focused more attention on the fireball/plume phenomena that had the greatest potential for being observable. By the time the comet arrived at Jupiter, there was general agreement among the impact modelers that (for sufficiently large impactors), debris ejected by the collisions would quickly rise above the Jovian limb into line of sight for Earth-based telescopes [51], [42], [1], [2], [3], [41]. A consensus was never reached, however, on how bright the fireballs would be, how high the plumes would rise, nor on how large the fragments would need to be to generate visible plumes. The uncertainty in plume visibility as a function of fragment size, coupled with the uncertainty in the sizes of the actual fragments [48], resulted in a spectrum of recommendations from modelers. In most cases, the impact models focused on fragment entry and early plume growth.

Astronomers indeed observed the fireballs and plumes predicted by the models, and in doing so transformed them from theoretical constructions to observational facts. The actual event, however, produced a much richer array of consequences than anyone had anticipated. Because of a massive international effort, an overwhelming amount of high-quality observational data was collected during the impact week. Some of the new phenomena were quickly explained and are fully consistent with the models; interpretation of other observations continues to require further analysis and synthesis of the data. Computational models continue to provide guidance and contribute to our understanding of this event.

Moreover, the simulations of the SL-9 impact — coupled with interpretations of the observational data — will ultimately enhance our ability to predict the consequences of a comet or asteroid impact on Earth, leading to improved risk assessments. This section briefly summarizes the most useful observations of the collisions, provides a description of our simulations, and outlines our current "big picture" interpretation. The framework presented here is an elaboration on and update of the scenario presented by Boslough et al. [4]. It is consistent with the consensus that was reached at the 1995 IAU meeting in Baltimore (summarized by Chapman [10]), and incorporates elements of models of Svettsov [74], Crawford [12], Fortov et al. [61], Mac Low [23], Zahnle [52], and others. This scheme attempts to conform with as much of the observational data as possible, and incorporates the most recently published observational interpretations. As with any working model, the details of the interpretations may evolve as the research efforts continue.
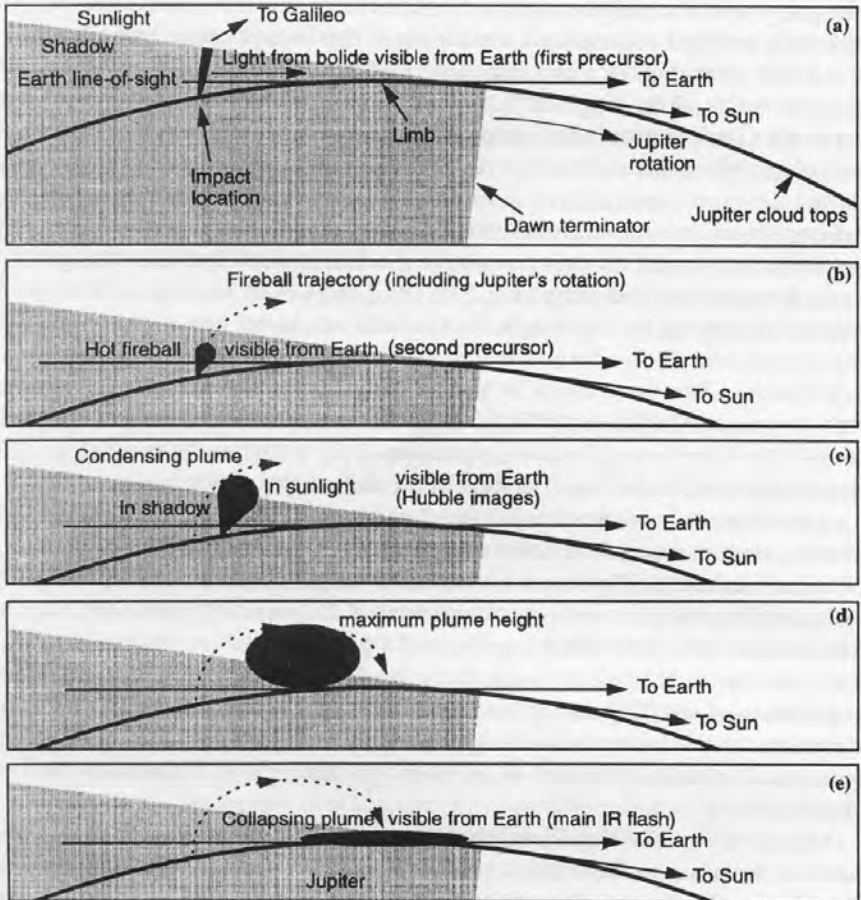
FIGURE 1. Geometry of impacts, just beyond Jupiter's limb (horizon) with respect to Earth: (a) Dust and main fragment enter Jupiter's atmosphere, generating entry flash; (b) incandescent fireball rises into view from Earth; (c) condensing plume ballistically rises into sunlight; (d) plume reaches maximum altitude of about 3300 km above clouds; (e) Plume collapses and rotates into view (modified from [3]).

SL-9 OBSERVATIONS

It turned out, by good fortune, that the geometry and timing of the series of impacts was nearly ideal for making useful observations from Earth-based instruments and from the Galileo spacecraft (Fig. 1). With the impact loca-

tion only a few degrees beyond Jupiter's limb, as predicted by dynamicists, the hot debris ejected by each collision had to rise only a few hundred kilometers to become visible. It could then be seen in profile, making it possible to observe its shape and size. The vantage point from Earth was close to perpendicular to the trajectory of the fragments, so that the effect of impact obliquity could be seen. Because the impact point was beyond Jupiter's limb, the arrival time of debris above the line-of-sight altitude could be measured for some of the fragments. Combining this information with the time of impact extracted from direct measurements from Galileo (and in some cases from Earth), the early fireball trajectory could be determined. The position of Jupiter (near quadrature) meant that the luminous debris was in shadow when it first rose into view, making it possible to estimate its brightness. This configuration also meant that additional trajectory information could, in principle, have come from the time of arrival of the fireball into sunlight. As the cold, condensed plume rose into the sunlight it scattered enough light to be imaged so that its projected shape could be determined, and out-of-plane morphological information could be extracted from the shadow-line on it. Furthermore, each impact site was on the side of Jupiter (near local dawn) that immediately rotated into view from Earth. This gave the fireball a velocity component toward the limb, and made it possible to observe the pattern of debris and wave phenomena immediately after impact, and for an entire Jovian half-rotation (from local Earth-rise to Earth-set) afterward. Finally, there wasn't just a single collision. A whole string of about twenty sizable fragments impacted at a rate of several per day for nearly a week, allowing observatories around the world to collect data with many types of instrumentation, thereby providing multiple chances to improve the observations and to employ different modes of data collection. These multiple opportunities were particularly fortunate for the Hubble Space Telescope (HST), which is in low-Earth orbit and blocked from viewing Jupiter about half the time. Likewise, the Galileo spacecraft was able to take advantage of several different data collection strategies. This nearly best-case impact situation — like a well-designed series of experiments — has allowed many direct comparisons to be made between simulations and observations. It would not have been possible if the vantage point had been different, or if there had only been a single event.

   The collision also took place at a time that was quite advantageous in terms of the instruments that could be used to make observations of the impact sites; the recently-refurbished Hubble Space Telescope (HST) and the approaching Galileo spacecraft were both available to complement the Earth-based observations in a way that would not have been possible only a year earlier. HST happened to be in position to capture direct images of the plumes from four impacts, and Galileo had a direct line of sight for all. HST images have provided information about the size, shape, evolution, and optical properties of the fireballs and plumes, and about the structure and evo-

lution of the impact sites after plume collapse [19], [63]. HST and Earth-based spectroscopy yielded evidence for water, ammonia, iron, silicon, magnesium, sodium, calcium, lithium, potassium, diatomic sulfur other sulfur compounds, carbon monoxide, and hydrogen cyanide at the impact sites [36], [55], [76], [24], [26], [39]. Galileo's Ultraviolet Spectrometer (UVS), Photopolarimeter Radiometer (PPR), Near-Infrared Mapping Spectrometer (NIMS), and Solid State Imaging camera (SSI) instruments provided precise timing for the entry of many of the fragments into the atmosphere, as well as information about the expansion rates, cooling histories, and upward velocities of the incandescent, ballistic fireballs [26], [6], [9], [20]. The event timing as determined by Galileo measurements has provided a strong basis for interpreting the multiple flashes observed from Earth in a way that is consistent with the computational models (Fig. 2).

PREIMPACT SL-9 SIMULATIONS

Crawford et al. [14] used the CTH Eulerian shock-physics code to simulate two- and three-dimensional representations of the impact events. The 2D computations were of the impactor penetration, simulating the entry, deformation and breakup of the comet fragments. The calculations were performed in a "reverse ballistic" sense using a Jovian atmosphere moving upward at 60 km/sec impinging upon an initially stationary fragment. The Eulerian mesh extended 100 km radially and 1000 km above and below the comet. The fragment was maintained in a high resolution portion of the mesh (equivalent to 25 computational zones across the projectile radius and extending 10 km vertically and 5 km radially) by Galilean transformations of the entire mesh every 0.1 seconds of simulation time. Zone size gradually increased away from the high resolution portion of the mesh to preserve all the materials of the calculation yet maintain computational efficiency.

The comet fragments in the simulations were composed of water ice with initial density and temperature of 0.95 g/cm^3 and 100 K, respectively, using tabularized version of the ANEOS equation-of-state which allows melting and vaporization [46]. The atmospheric stratigraphy in the calculations matched Voyager data for Jupiter at high altitudes (Orton, unpublished data) and extended adiabatically to lower altitudes. The atmosphere consisted of 89% hydrogen and 11% helium at all altitudes and was modeled with a tabular equation-of-state allowing dissociation and ionization [21]. It was scaled vertically by a factor of 1.41 (to account for the approximate 45° entry angle) and inserted into the lower portion of the computational mesh. The atmosphere propagated into the upper portion of the mesh as the comet deformed and broke up in the higher-pressure regions of the lower atmosphere.

Hypothetical view from Earth
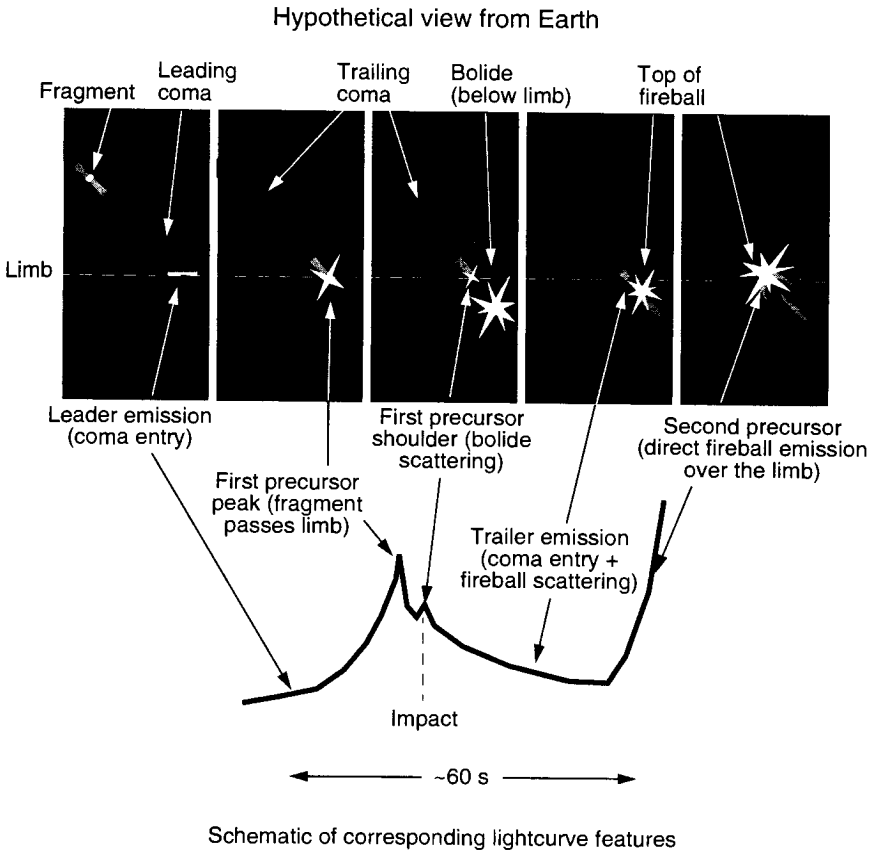

Schematic of corresponding lightcurve features

FIGURE 2. Cartoon of the first minute of impact phenomena as observed from Earth, relating events at the limb of Jupiter to an idealized high-resolution lightcurve. Only light radiated or scattered from above the limb was detected on Earth.

Before the impacts, we focused our attention on modeling large fragments with diameters between 1 and 3 km. This is the size range bracketed by the most optimistic preimpact estimates (summarized by Weaver et al. [48]), and would be more likely to yield observable phenomena than smaller fragments. During entry into the low density outermost reaches of the atmosphere, the projectile forms a clean bow shock. Atmospheric temperatures at the leading edge of the projectile reach values as great as 35,000 K. During deformation, the projectile thins and the leading edge flattens. Acceleration instabilities develop in a manner described by Swegle and Robinson [43]. Eventually, projectile thinning meets with the growing instabilities and breakup occurs. During penetration, the projectile continuously gives up kinetic energy to heating and deflection of the Jovian atmosphere (a relatively small amount goes toward internal heating of the cometary constituents).

Crawford et al. [14] determined the total energy deposited by hypothetical 1, 2, and 3 km diameter cometary fragments during their penetration of the Jovian atmosphere. An important result for fragments between 1 and 3 km in diameter was that most of their kinetic energy and mass was deposited beneath Jupiter's outermost visible cloud layer, which is about 10–20 km above the reference altitude at 1 bar. For the 3 km diameter fragments most of the impactor's mass is deposited at depth, and less than 1% is entrained in the upwardly growing fireball. Crawford et al. [14] also investigated the influence of fragment body shape on the energy deposition profile, and tested for sensitivity to numerics by performing the same calculations with different resolutions.

For the 3D calculations, the results from the two-dimensional entry, deformation and breakup studies were inclined at 45° and mapped into a three-dimensional representation. Three-dimensional, bilaterally symmetric simulations most accurately rendered fireball evolution beginning about 10–15 seconds after first contact of the fragment with Jupiter's atmosphere. Density, temperature, fluid velocity, and pressure of the cometary debris and shocked Jovian atmospheric constituents were preserved in a spatially average sense while total energy was conserved. Some calculations were allowed to evolve for up to 120 seconds. Generally, the simulation results indicated that early-time fireball growth is predominantly directed outward along the incoming bolide trajectory but is redirected, at later time, towards growth dominated by the vertical gradient of the Jovian atmosphere.

In an attempt to attain adequate resolution for these large fireball simulations, the calculations were performed on the 1840-processor Intel Paragon massively parallel supercomputer at Sandia National Laboratories. The simulation of the fireball formed by the impact of a 3 km comet fragment consisted of 8 million 5 km cubical zones. Lower energy events, formed by the impact of 1 or 2 km fragments, were modeled with more finely resolved, but less spatially extensive, simulations. More recent 2D simulations indicate that these preimpact 3D simulations were somewhat under-resolved, despite having been carried out on the world's most powerful computer. The qualitative aspects of the simulated fireballs and plumes remain valid, but the lack of sufficient resolution limited their quantitative accuracy, and under-predicted the ejection velocity of material during early fireball growth.

In the 3 km simulation, the fragment deposited (as internal energy of H_2, He and H_2O vapor) more than 95% of its kinetic energy (6 million megatons) during its penetration of the Jovian atmosphere (a comparatively small amount remained as kinetic energy of cometary water vapor). The resulting fireball and surrounding shock wave is shown in cross-section, 67 seconds after impact, in Crawford's Fig. 1 [58]. The spherical shock wave is advancing upward at a velocity of 25 km/sec. It has reached a diameter of 700 km and an altitude of 900 km above the clouds. For reference, the Jovian cloud tops are located at an altitude of 10–20 km and the projection of the limb of

Jupiter (as seen from Earth) varies as a function of impact location. The limb projections for impacts occurring 4 and 6 degrees beyond the limb were at 200 and 400 km altitude, respectively. The fireball itself is a rapidly rising cloud of cometary debris and Jovian atmosphere at high temperature. About a minute after the impact of a 3 km cometary fragment, the fireball is still at 1700 K, and the shock wave temperature is 2300 K. An optically-thick fireball would have had an apparent bolometric magnitude (as viewed from Earth) of about 2 at this time. The observed fireballs were significantly dimmer, implying they were not optically thick and/or that the fragments were smaller than 3 km in diameter.

The term "fireball" refers to the mass of hot gases consisting of a mixture of Jovian atmosphere and cometary material that is ballistically shot upward by the impact. In the first moments after impact it is very hot, incandescent, and radiating in the visible and near infrared. The fireball is preceded by the "entry flash" or "bolide" phase, during which time the comet fragment (and associated debris) deposits its energy in Jupiter's atmosphere. The entry flash as seen from Earth may be dominated by the deposition of energy at very high altitude (above the limb) by small particles in the coma surrounding the main fragment, and for that reason its use as a timing fiducial is not as straightforward as we had hoped [2]. The main fragment mass does not begin to deposit a large amount of energy until it has passed beyond the limb, after which it begins to heat an entry column of atmosphere as it loses its kinetic energy. It is that column of gas that explosively expands and becomes the fireball. The word "plume" describes the debris cloud after it has expanded, cooled adiabatically, and begun to condense. Clearly, there are no precise temporal demarcations separating bolide, fireball, and plume phases, but various well-defined "events" associated with these phases, and related to the viewing geometry, can be extracted from the best time-resolved lightcurves (Fig. 2).

The differences between the fireballs described here, and other closely-related phenomena should be understood. Analogies to the fireball associated with the detonation of a nuclear device are limited. The development of a nuclear fireball is dominated by interior radiative transport at temperatures of tens of millions of degrees. Some fraction of this energy forms a shock wave in the atmosphere, which separates from the fireball but can still be luminous if strong enough. The shock wave generated by the impact fireball is similar to the outer, mechanically-driven nuclear blast wave. However, the temperature of a shock wave can be much higher at a given propagation distance from an impact that is a million times more energetic than a megaton-scale nuclear device. The fireball itself is a ballistically-rising mixture of shocked atmosphere and vaporized cometary material. A nuclear fireball that is small compared to the scale height of the atmosphere will be driven upwards by buoyant forces because it is less dense than the surrounding atmosphere. This upwelling gives rise to the toroidal "mushroom cloud" usu-

ally associated with atmospheric explosions. A large impact fireball can be much greater than the scale height of the Jovian atmosphere. Because the atmospheric pressure is much greater at the bottom than at the top, it is contained at depth and relatively uncontained at altitude. It, therefore, accelerates upwards as if shot from a gun. Simulations and observations indicate that later, when most of the fireball mass is unconstrained, it begins a more homologous upward expansion. Even though its density is much greater than the surrounding atmosphere at the top, its inertia will carry it on a ballistic trajectory which rises as much as several thousand kilometers above the clouds.

POSTIMPACT SL-9 SIMULATIONS

Subsequent to the collision, Crawford [12] has improved the computational models by developing an analytical entry model that allows the numerical simulations of the fireballs and plumes to be initialized without having to perform a computationally-intensive hypervelocity entry simulation every time. This paper showed that previously-ignored radiative ablation makes a significant contribution to the rate at which energy and mass are deposited at high altitude, which controls the formation and early evolution of the fireball. By performing a large set of two dimensional simulations, Crawford [12] called into question our earlier interpretation of a fireball that transforms directly to a plume as it grows, cools, and condenses. Instead, the early, incandescent "entry fireball" grows from and expanding entry column, fades, and becomes transparent before it reaches an altitude of 6,000 to 10,000 km. Imbedded within the fireball, however, is material excavated from deeper within Jupiter's atmosphere, which condenses to form the visible outer surface of the plume that rises up to about 3,000 km.

One key result of this paper was an explanation for why all the observed visible plumes rose to about the same height. Both the energy deposited per unit distance along the path, and the mass into which it is deposited, are proportional to a projectile's interaction cross-section. The energy density within the entry column is therefore independent of fragment size down to the depth at which its velocity begins to appreciably drop off. Since the expansion of the hot vapor in the column converts internal energy of each packet of mass to gravitational potential energy, the maximum height each packet reaches is independent of fragment size, as long as it comes from above the level at which the fragment begins decelerating. If this level is beneath the cloud layer that forms the visible envelope of the plume, the plumes will all appear to rise to the same height. The threshold diameter above which fragments will penetrate the ammonia clouds before slowing appreciably yields the lower limit for the size of the fragments that generated the high plumes. According to Crawford [12], this lower bound is about 200 m.

The most recent computational models [58] have provided another means for estimating the size of individual comet fragments, by determining light emission from the impacts as a function of time and viewing geometry. By varying parameters and comparing the synthetic lightcurves to those record-ed by instruments aboard the Galileo Spacecraft, the sizes of five fragments were estimated. These values were correlated with HST images and Earth-based photometry to arrive at approximate sizes for the other largest frag-ments, which in turn allowed an overall progenitor diameter to be deter-mined assuming a density for SL-9, based only on the impact flash. For densities of 0.25 and 0.50 g/cm^3, the best estimates are 1.8 km and 1.4 km, respectively.

SL-9 INTERPRETATIONS

Figures 1–4 are schematic portrayals of the sequence of events associated with an idealized SL-9 impact. These representations are inferred from the composite of Earth-based photometry data, Galileo lightcurves, and HST imagery. Figure 1 depicts a side view, looking from a direction perpendicu-lar to the line between Jupiter and Earth. Figure 2 is a cartoon depicting the view from Earth during the first minute or so, with the features of a generic high-resolution lightcurve identified with various events at the limb. The lightcurve is modeled after the time-resolved data collected at 2.3 μm from the L impact by Hamilton et al. [64] at Calar Alto Observatory, Spain. Figure 3 is a plan view of the impact site from a stationary (nonrotating) vantage point, with snapshots of a map projection of the evolving impact sites at var-ious time steps after impact. As the point of impact rotates from west to east, it moves from left to right in the stationary field of view of the illustration. Jovian north is up; the approximately vertical lines represent the minimum line-of-sight altitudes to the Earth and Sun. The figure is not intended to de-pict the exact geometry, nor is it supposed to represent a particular impact, but is a composite of features observed from various events. Figure 4 shows a simplified side-view of the fireball/plume evolution. In reality, the ejecta cloud is not a discrete packet, but a continuum with widely varying temper-atures, densities, and pressures. As described earlier, the impacts were not "clean experiments," but probably involved closely-spaced multiple impac-tors embedded within a dusty, light-scattering cloud of smaller particles (co-ma), which also had a hypervelocity, light-producing interaction with Jupiter's atmosphere.

In the Fig. 3 inset are some idealized examples of Galileo and Earth-based lightcurves. The Galileo PPR curve is based on the measurements of several impacts at 945 nm [26]. Since Galileo had a direct view of the impact, the sharp rise in the PPR curve defines the time of impact for the events for which PPR data were collected (UVS and SSI instruments on Galileo deter-

mined timing for some of the other impacts; see Chodas and Yeomans [11] for precise timing information). The upper Earth-based lightcurve is a schematic adaptation of data at 3.5 μm collected at the Palomar Observatory by Nicholson et al. [35] for the R impact; qualitatively similar curves were obtained by Graham et al. [18] at 2.3 μm with the Keck Telescope, and for the K impact at 2.35 μm at the Okayama Astrophysical Observatory by Takeuchi et al. [45]. The lower curve is based on 10 μm data collected at the European Southern Observatory by Livengood et al. [22].

The following is a generic description of the sequence of events, with letters corresponding to those in Figs. 3 and 4. The various phases are defined primarily for conceptual purposes; there are not distinct boundaries between them, and in many cases they overlap. Approximate times are given relative to fragment impact time (defined as its arrival at the 100 mbar level by Chodas and Yeomans [11]. These descriptions relate the phenomena associated with each phase to corresponding observational data that were collected from at least one of the impacts, acknowledging the fact that a different suite of instruments was used for each impact, and that some impacts were too weak to be observed. In reality, every impact has its own unique set of data.
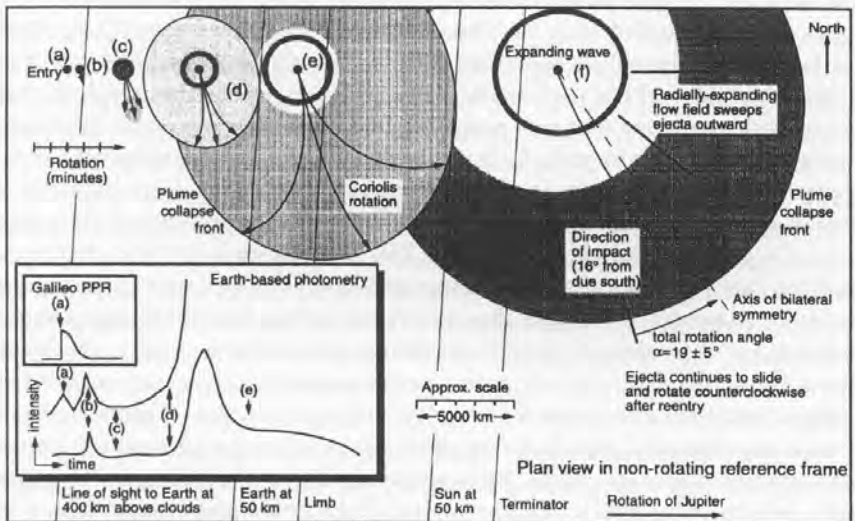

FIGURE 3. Plan view (map projection) of idealized impact site from a stationary (non-rotating) vantage point, with snapshots of a planar projection of its evolution, interpreted using the conceptual framework provided by computational simulations. This figure schematically represents features that were seen after several of the larger impacts. See text for detailed explanation (from [4]).
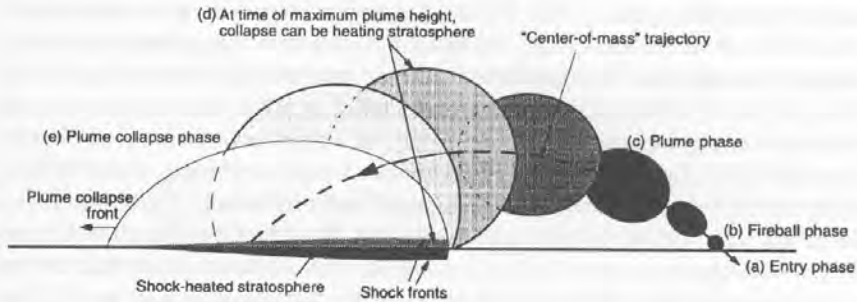
FIGURE 4. Side view of highly idealized fireball/plume evolution which leads to a "hypervelocity splat" when the plume collapses, heating Jupiter's upper atmosphere over a very large area. This schematic shows the ejecta cloud as a discrete packet, rather than the continuum it really is (modified from [4]).

A. Entry Phase (Preimpact to 10 or 15 Seconds)

A fragment (or tightly-spaced cluster) enters Jupiter's atmosphere, depositing energy and leaving a debris column that consists of a mixture of Jovian atmosphere and cometary vapor at high temperatures and pressures. Thermal radiation from this column is dominated by the very high temperatures at the front of the bow shock before it drops beneath the uppermost cloud layer, and is seen directly in the ultraviolet, visible, and infrared wavelengths by Galileo's detectors, which recorded color temperatures of around 8,000 K during this first part of the entry phase for the G impact [20]. The temperature of the column at a given point along the trajectory of the fragment begins to drop as soon as the energy is deposited into the bow shock, and it immediately starts its expansion. As the entry phase continues beneath the clouds, where kinetic energy of the fragment is converted to internal energy, the upper part of the column begins its expansion into an incipient fireball. The emission during the entry and early fireball phase, as viewed from Earth, was complicated by viewing geometry and scattering effects. But since time-resolved data were collected with a direct view by Galileo's instruments, they can be compared directly to theoretical lightcurves to provide estimates of fragment sizes. This aspect of the data is thoroughly discussed by Crawford [58].

In some cases the onset of the emission seen from Earth was not sudden, as would have been expected for a single fragment, but exhibited a gradual increase in intensity (the "leader" [35]). The best explanation for the leader is the hypervelocity collision of the leading part of the coma into Jupiter's upper atmosphere. Because the small particles that make up the coma are so far ahead of the main fragment, they begin to impact Jupiter many seconds — or even minutes — in advance. McGregor et al. [70] determined that the

time-resolved infrared emission at 2.34 μm, from the vicinity of the limb just above the impact point of G and K fragments, began to rise above background levels at about 1.5 and 3.5 minutes before fragment impact, respectively. This implies that localized meteor storms were becoming bright enough to be seen from Earth when these two fragments were still at respective distances greater than 5,000 and 12,000 km from their point of impact (Fig. 2). The 2.3 μm lightcurve [64] shows a leader beginning about 30 seconds before the peak, when the L fragment was still nearly 2,000 km above the cloud tops. These distances are much less than the total length of the comae, which had been stretched out to lengths tens of thousands of kilometers in their approximate direction of motion as the fragments neared Jupiter due to differential acceleration by the planet's gravitational gradient [48].

The shape of the first precursor probably has more to do with the density profile of the stretched-out coma than with anything else. The Earth-based data [64] were collected from the L impact with sufficiently small sampling intervals (1.2 seconds) to resolve the structure of the coma on a spatial scale of less than 100 km as it collided with the rarefied upper reaches of Jupiter's atmosphere at 60 km/sec. At any instant in time, the emission from the entering coma as seen from Earth is dominated by meteors within a scale height of the line-of-sight altitude above the limb (about 350 km above the clouds for the L impact) so the time-resolved emission is proportional to the number of meteors passing through that altitude, assuming a uniform size distribution. The main peak in the L lightcurve has a half-height width of about 12 seconds, which is consistent with a debris cloud having a density concentration within about 700 km along the direction of motion. This peak appears 8 seconds before the impact time as determined by Galileo instruments [26], precisely when the main fragment was passing the limb at about 350 km altitude. A second, smaller peak in the first precursor of the L lightcurve appears within one sample interval of the Galileo impact time, when the bolide is at its brightest just before reaching the cloud tops. This short, bright entry flash would not be visible from Earth unless there were still scattering material above the limb at the same instant. The fact that the first peak had not yet disappeared by this time implies that the densest inner part of the trailing portion of the coma was still crossing the limb at the time of impact, providing a scattering medium in Earth's line of sight.

The "trailer" of the first precursor probably contains contributions from both the trailing portion of the coma generating high altitude line-of-sight meteors, and the same portion of the coma scattering light emitted from the fireball rising from beneath. There are many complications due to multiple sources and dependence of scattering and emission on the details of the unknown density profile of the coma in the immediate vicinity of the main fragment. Thus, the structure and intensity of the first precursor in Earth-based lightcurves cannot be used to determine fragment properties. More-

over, only the L lightcurve [64] is sufficiently well resolved to distinguish the limb-crossing coma peak from the bolide flash peak. In many of the lightcurves, these two events are unresolved, and together form the "first precursor." In other lightcurves, no first precursor was observed at all. A reasonable explanation is that in addition to depending on wavelength, sampling interval, and sensitivity, its presence depends on coma density and location of impact point beyond the limb. The latter is important because it determines the altitude and density of the atmosphere into which meteors form in line of sight from Earth, and dictates the distance between the bolide and the scattering medium.

B. Fireball Phase (5 or 10 Seconds to 3 or 4 Minutes)

After energy is deposited in the wake of the fragment, the column explosively expands upward and outward along the atmospheric density gradient, cooling isentropically as it rises. The expansion begins instantaneously, before the entry phase is complete. This cooling is seen by Galileo instruments as a decrease in radiative intensity, and a shift toward longer wavelengths in thermal emission. In the infrared, the NIMS data exhibit a decrease in the intensity of methane absorption bands with time for the G fireball, consistent with a rapidly rising light source within Jupiter's atmosphere. Carlson et al. [6] used these time-dependent absorption band changes to determine that the vertical velocity component of the main near-infrared light source from the G fireball had reached 2–3 km/sec within 20–30 seconds of impact.

Computational models show that the fireball growth is not a simple isotropic expansion, but that it starts near the tropopause and is guided up the high-temperature, low-density, radially expanding entry column [12], with an appearance reminiscent of the inflation of a long narrow balloon. In less than one minute or so, the incandescent fireball rises to a few hundred kilometers and becomes visible from Earth, appearing as a second precursor in some photometry data. The exact timing depends on both the point of impact and on fragment size although the most recent models suggest that, over the range of sizes of the fireball-producing SL-9 fragments. the latter dependence is weak [58]. The entry fireball is preceded by several seconds by a shock wave. Earth-based detection of this shock would have provided further validation for the computational models, but it was either too weak to have been seen as an independent precursor, or else it was simply unresolved. In the absence of a nearby light-scattering medium, the arrival time of hot material above the Jovian limb would have been seen as a sudden increase in the lightcurve. In many cases the second precursor was not sharp, suggesting that the sudden fireball arrival was preceded by a more gradual increase in light scattered over the limb. The most likely source of light is from the rising fireball itself, before it reaches the altitude where it can be seen directly. The most probable light scattering material that would be

above the limb at this time (and close to the light source) would be the trailing part of the coma. Some of the lightcurves exhibit sharp second precursor onset — such as is the 2.3 μm L data [64]. At this time, the rising fireball approaching the limb is colliding head-on with the descending coma that had been trailing the L fragment by about 2,300 km. After this early fireball rises above the limb, it continues to grow and cool, leading to a trailing off of the second precursor.

Information about the Earth-based field of view during the entry and early fireball phases for various impact locations can be extracted from Fig. 5. The line-of-site altitude from Earth at a spot directly above the impact point is plotted as a function of time for various fragments. As the rotation of Jupiter brings the impact point closer to the limb, the line-of-sight altitude moves lower, so the curves (provided by Paul Chodas, personal communication) are decreasing functions of time. We originally used this diagram to argue for the visibility of fireballs by plotting ballistic trajectories extrapolated from our 3D shock physics simulations [2], and showing that for impactors greater than 1 km in diameter, fireballs would rise above the line-of-sight altitude within a few minutes. More recent, higher-resolution 2D simulations by Crawford [12] has revealed that our original 3 km fireball trajectory was about right, but that our 1 km trajectory was too low due to insufficient numerical resolution. Furthermore, these simulations demonstrated that plumes from impactors greater than about 200 m in diameter should all rise to about the same height, so the ballistic trajectories would all be about the same. Their time of arrival above the limb would therefore be insensitive to fragment size for a given impact geometry, in contradiction to our expectations [2]. When the calculated trajectories are plotted on this diagram, their intersection with the line-of-sight curves should define the times of arrival of the plume-forming surface above the limb. If that same surface evolved from the leading edge of the incandescent fireball, then the beginning of the second precursor (in the absence of scattering) should appear at this time. However, the second precursor start times extracted from a compendium of measurements [11] do not show any clear correlation. This inconstancy may be the result of a combination of light scattering and limited temporal resolution.

The Hamilton et al. [64] lightcurve at 2.3 μm for the L impact provides the best published example of an emergent second precursor with good time resolution. This precursor starts about 36 seconds after impact, which is about 14 seconds before the visible plume-forming surface reaches line-of-sight. Our early work suggested that it was the expanding debris front that defined both the leading edge of the incandescent fireball at early times, and the top of the plume at late times [4]. This L lightcurve, however, strongly supports the Crawford [12] view that the top of the incandescent "entry" fireball precedes the visible plume to that altitude, and later becomes transparent, with the visible plume embedded inside.
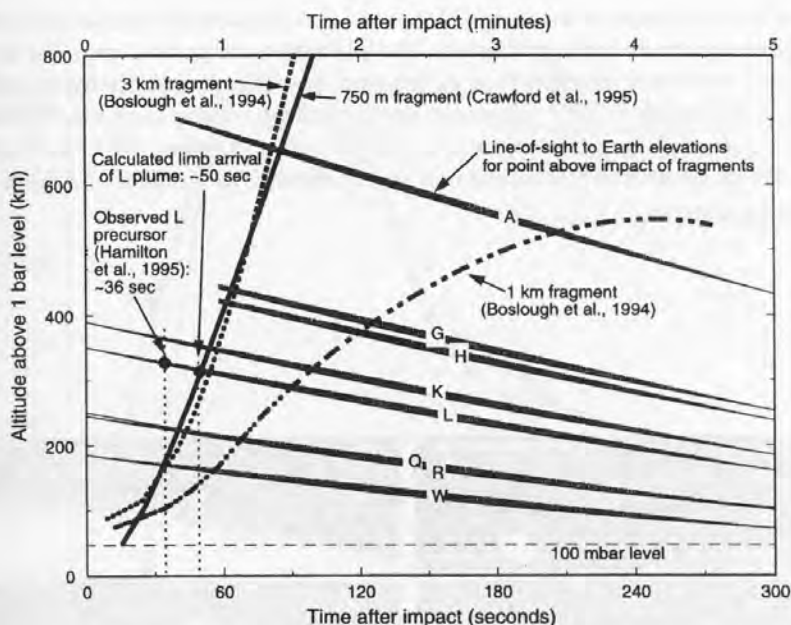
FIGURE 5. Calculated trajectories of fireballs from 3D simulations for 1 and 3 km diameter ice fragments [3], and for a 750 m diameter fragment [12]. Approximate line-of-sight elevations to the Earth are based on the impact location for several fragments (identified by letter).

C. Plume Phase (3 or 4 Minutes to 10 or 15 Minutes)

The debris continues to rise ballistically. It expands and cools, and begins to condense. Crawford [12] favored the idea that the outer surface of the visible plumes was mapped from a horizontal surface near the cloud tops of the preimpact atmosphere. In this view, the visible surface of the plume is a condensation surface derived from the Jovian clouds. In the most recent models [58], it appears that the surface translated by the explosion from a region near the tropopause is accompanied by a steep density and temperature gradient. The opacity that gives definition to the plumes may be due to a threshold density of particles of condensation. This would imply that the visible plumes were rather diffuse, and supports the view that they were actually nested within a transparent plume that rose to much greater altitudes. The outer, transparent layers would be derived from the debris in the upper part of the entry column which defined the hot, incandescent entry fireball. When the visible plume reaches an altitude greater than one or two thousand kilometers (depending on the point of impact), it enters sunlight. We had anticipated that this would be detectable from Earth, and would provide another

point on the ballistic trajectory [3], but the precise sunlight arrival time was not obvious from the lightcurves. The plume's emergence from Jupiter's shadow, however, enabled it to be imaged for several impacts by the HST [19]. A sequence of HST images of the growth and collapse of the G plume over a period of about 20 minutes is shown in Fig. 6, along with the results of a 3D simulation of fireball/plume evolution after the impact of a 3 km diameter fragment.
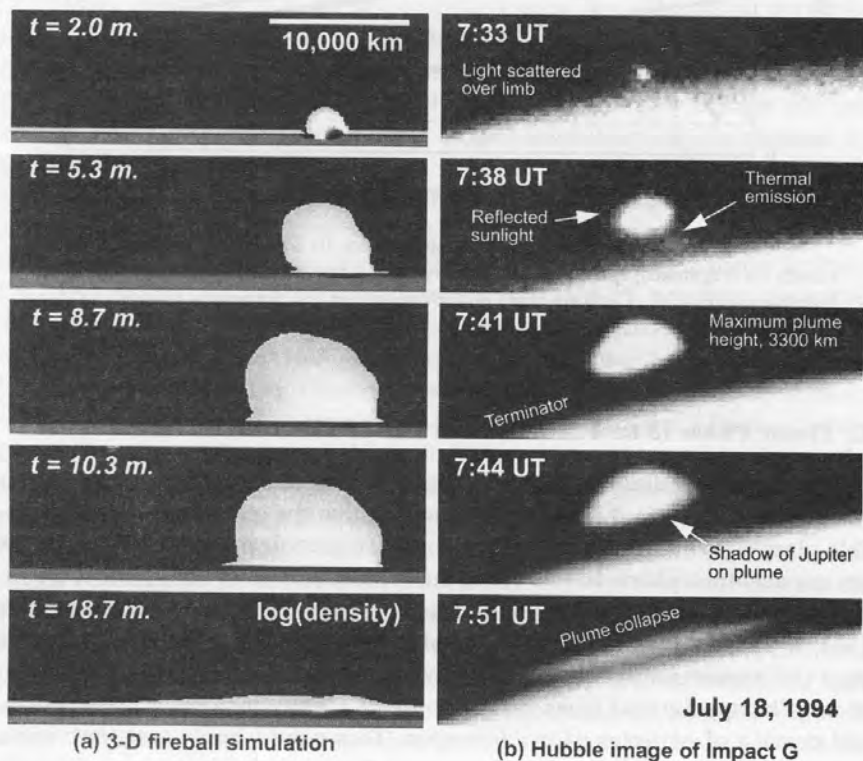

FIGURE 6. (a) Simulation of 3D fireball/plume evolution after the impact of a 3 km diameter fragment. Shading indicates log (density) with a cutoff at $10-12$ g/cm^3; times are in minutes after impact (from [15]). (b) Sequence of G plume images collected by Hubble Space Telescope (from [19]).
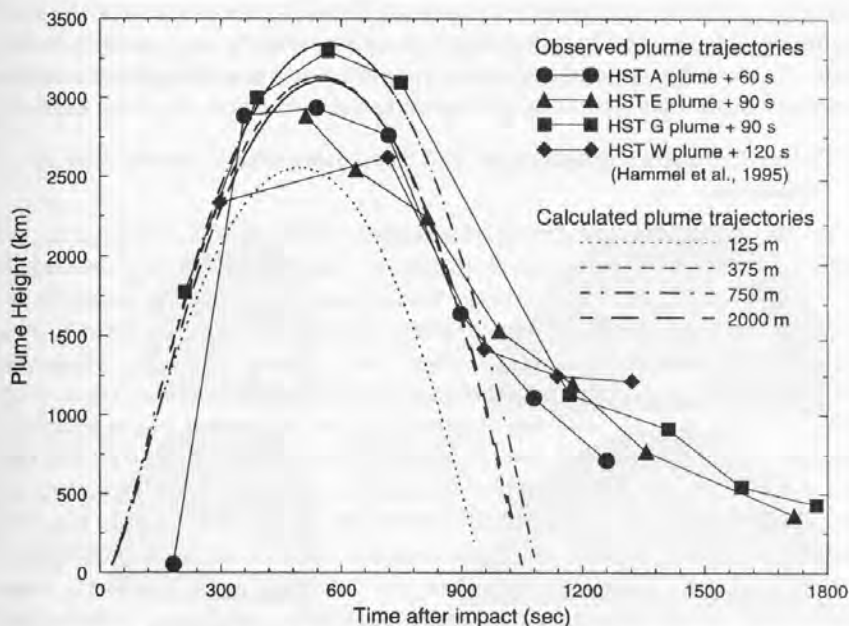
FIGURE 7. Plume heights determined from the Hubble Space Telescope as a function of time [64] plotted along with plume heights determined from a ballistic extrapolation of material ejected by impactorts of various sizes.

D. Maximum Height (about 9 Minutes)

At six minutes after impact, the plume is still growing to its maximum height, according to HST images. At this time, the lower part of the plume begins to collapse and heat Jupiter's stratosphere to a sufficiently high temperature over a large enough area that its emission begins to appear as the "main event" in both Earth-based [18], [34] in and Galileo NIMS [6] light-curves. Because the plume is still expanding as it rises, the collapse phase can actually begin before the top of the plume reaches its maximum height (Fig. 4). Figure 7 plots the altitude of the highest tracer particle derived from the 1 bar level, as a function of time, for impactors of four different sizes simulated by Crawford [12]. This figure demonstrates how insensitive the maximum plume height is to fragment diameter once a threshold about 125 m is reached. Even though the plumes were ejected along the entry track at an angle of 45 degrees, they also expanded laterally away from the track, and upward, so the that tops of the visible plumes were not comprised of the material that was ejected at highest velocity with a horizontal component. Since the top of the plume is defined by a slowly rotating surface, its position is not described by a single Lagrangian point on a ballistic trajectory; however, the difference is minuscule. The plume heights determined from HST images [19] are also plotted in Fig. 7, with the time scales shifted to optimize their

alignment with the calculated trajectories. The differences between the HST plume heights and the calculated ballistic plume height are probably attributable to a combination of variable sensitivities and wavelengths, as well as exposure times that were long compared to the timescales of plume motion.

E. Plume Collapse (Splashback) and Transition Phase (about 5 to 15 Minutes)

As the still-expanding debris cloud begins to fall back, it compresses and heats a large area of the Jovian stratosphere. The heated region grows rapidly. The peak of the main event in the Earth-based lightcurves is probably determined by a combination of competing effects, including increasing area, radiative and decompressional cooling, and viewing geometry. However, Nicholson [35] and others have pointed out that the data of McGregor et al. [70] and Lagage et al. [69] demonstrate that the main event began about six minutes after impact in all cases, regardless of viewing geometry. The fact that this six-minute interval before the main event is an intrinsic property of the plume collapse was later confirmed by the Galileo NIMS data [6]. The most reasonable explanation for a six minute interval has been provided by Zahnle [52], who suggested that there is a threshold vertical velocity component that the re-entering plume must reach before the shock temperature is high enough to synthesize the organic compounds that serve as the required opacity source for emission. This threshold velocity is about 4–5 km/sec, which is reached after about six minutes.

Another transition takes place near the peak of the main event, and was observed as an emergent CO emission band 12 minutes after the K impact in the spectral data at 2.3 μm by Meadows and Crisp [79]. Excitation of this band requires a temperature of at least 2000 K, which implies that it must be coming from the shocked layer where the plume is collapsing onto the top of Jupiter's atmosphere. Nicholson [35] attributes its sudden appearance to the time at which the vertical component of the plume re-entry velocity approaches 9 km/sec. That explanation, however, may not completely account for the suddenness of its onset, which may be alternatively explained by a morphological transition associated with the plume collapse process (Fig. 8). When the plume is growing, it consists of nested shells of Jovian atmosphere derived from various initial depths. As it begins to collapse, the outer shells collide with Jupiter's atmosphere first, and a zone of inverted stratigraphy begins to grow laterally uprange from the point of impact. These collapsed layers maintain their horizontal velocity and slide outward before losing their kinetic energy by dissipative processes. Since the collapse zone is shocked, it radiates at a much higher temperature than the surrounding plume, but because the outermost visible shell of the plume has some degree of opacity, this source is obscured. As the plume continues to collapse, a time is reached after which the outer shell folds back upon itself and remains upright, and the collapse front begins to recede from the outer limit of the collapse zone, ex-

posing it to view from outside and above. This is the time at which observers could expect to see a rapid increase in radiation from the collapse zone, and might explain the rapid onset of the hot CO emission band.
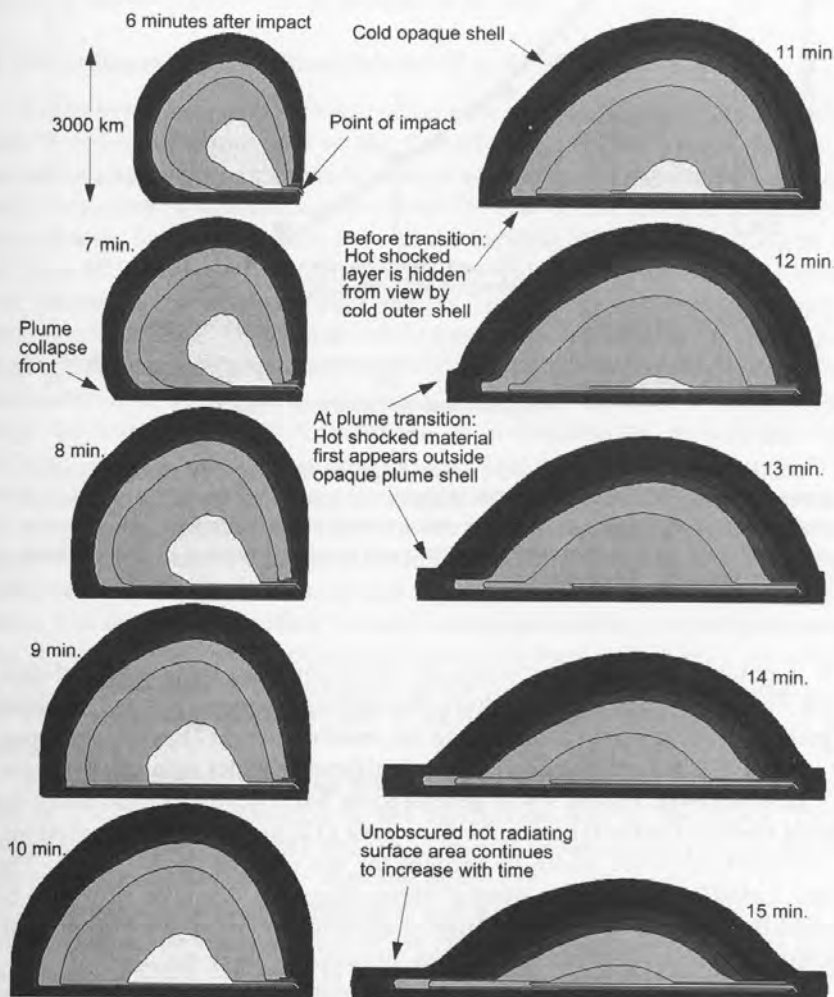

FIGURE 8. Rotated ballistic extrapolation of the ejected shells of material from the Crawford [12] 2D fireball simulations of a 1 km fragment, showing that a morphological transition takes place between 10 and 11 minutes after impact, when the leading edge of the collapse front begins folding back on itself, exposing high temperature shocked material to view from above. The collapse zone is vertically exaggerated in this figure to show how the atmospheric layers that re-enter before the transition are inverted.
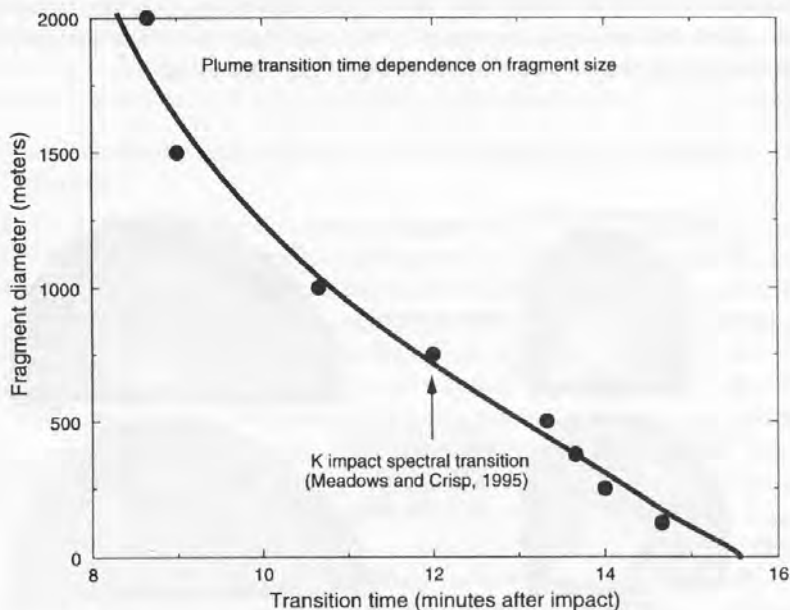
FIGURE 9. Transition time plotted versus fragment size, based on ballistic extrapolations of rotated 2D simulations. This dependence is primarily due to the variation of plume shape with impactor size, but the actual numerical relationship between diameter and transition time may depend on 3D effects and on precise position of the outermost opaque layer within the plume.

It is notable that this morphological transition time has a strong dependence on plume shape, which in turn depends on fragment sizes. The larger fragments produce wider plumes than the smaller ones [12], which is apparent in the HST images (the G plume is significantly wider than the W plume, for example [64]). Figure 9 was generated by ballistically extrapolating the ejected shells of material from the Crawford [12] series of 2D simulations, in a rotated reference frame to account for the oblique impact angle. The plume transition times were plotted versus fragment diameter. It would be premature to use this curve with high confidence to determine fragment diameters from observed transition times, because so many assumptions (e.g., origin depth of outer opaque layer) and approximations (e.g., rotated 2D simulations) were involved. However, there is a strong dependence of transition time on diameter, which suggests that a refined curve based on 3D simulations will ultimately be useful in providing an independent determination of fragment sizes. It is encouraging that the observed K transition time of 12 minutes yields a fragment diameter of 750 m, within the uncertainty of the estimate based on synthetic lightcurves [58].

After the primary peak in the main event appear subsequent shoulders and smaller peaks. In the infrared lightcurves of Nicholson et al. [34] and Graham et al. [18], these arise about 10 minutes after the main peak, and are almost certainly due to a much smaller, second compression of the atmosphere after the plume rebounds from the first collapse with a 10 minute period [16], [23]. This is followed by a third, and perhaps even a fourth bounce seen in the R impact lightcurves of Graham et al. [18].

F. Postcollapse "Splat" Phase (about 15 to 45 Minutes)

As the expanding debris cloud collapses it rotates counterclockwise in Jupiter's reference frame, due to the Coriolis Effect. This causes the ejecta footprint's symmetry axis to rotate out of alignment with the incoming fragment trajectory, which approached from 16° east of due south in Jovecentric coordinates. Since the highest parts of the ballistic plumes had as long as 18 minutes of flight time (Fig. 7), they rotated with respect to Jupiter by about 7.5° before re-entering. However, the HST image of the G impact reveals a total rotation of 23° [19] which would have required another 30 minutes of flight. However, one would not expect a fluid plume, collapsing onto a fluid atmosphere, to immediately decelerate, or "stick." Because it lands with a high horizontal velocity component, it maintains its momentum and "slides," continuing to rotate counterclockwise with respect to Jupiter. The total rotation angle of 23° actually implies a slide time of much greater than 30 minutes, because the mean sliding velocity was less than the re-entry velocity owing to its ultimate deceleration to a stop. This postcollapse rotation indicates that the ejecta blanket also expanded radially by the same mechanism. The outwardly-directed velocity component sets up a radially-expanding flow field that sweeps condensed matter outward, which may contribute to the crescent-shaped postcollapse debris pattern. This pattern remains to be fully explained, however, and is likely related to the structure of the plume itself [58].

A linear, radially expanding wave is made visible by an unknown mechanism, possibly condensation in the rarefaction part of the wave. These waves were observed in HST images of several impact sites as rings expanding at a constant velocity of 450–500 m/sec [19]. They have been modeled as inertia-gravity waves by Ingersoll and Kanamori [66] who predicted an enrichment in the water content of the troposphere by as much as ten times the solar abundance in order to explain the high wave velocities. However, the Galileo probe subsequently showed that Jupiter's atmosphere is too dry to support this model, hence this phenomenon remains unexplained. An alternative model of Zahnle [52] involves impact debris which is caught up in breaking nonlinear stratospheric waves. As the wave expands, the debris surfs along in front for thousands of kilometers, but slows down to a velocity below what was observed.

G. Aftereffects (Minutes to Hours)

The computational models indicate that there is also an upwelling phase. Careful examination of the 3D simulations of Crawford et al. [14] reveals that for massive, deeply-penetrating impactors, a bubble (or several bubbles) of hot Jovian atmosphere mixed with cometary vapor rises buoyantly from the depth of maximum energy deposition. This is between 200 and 300 km beneath the 1 bar level for 2–3 km diameter fragments. At 82 seconds after impact for a 1 km impactor there are three or four instabilities developing between about 50 and 200 km below the 1 bar level. At this time, they are 20–30 km in diameter, and have risen by about that distance from their starting point. These bubbles are analogous to buoyant nuclear explosion fireballs. Extrapolation of their upward motion suggests that they will begin arriving at the ammonia cloud layer within minutes, after having adiabatically expanded to many times their size. The resulting massive displacement of atmosphere is a likely source for the expanding wave, perhaps enhanced by a release of the latent heat of condensation of the entrained water vapor as suggested by Zahnle [52]. The upwelling might also manifest itself as thermal brightening or appearance of new spectroscopic signatures at the impact sites. It may be possible to extract information about the penetration depth (and therefore fragment mass) from the timing, temperature, and composition of any buoyantly-upwelling material.

Another late-time phenomenon was the giant ring that was observed at 3–4 μm by McGregor et al. [70], following two or three of the impacts. These rings continued to expand for up to 2 hours after impact, and were seen propagating as far as 18,000 km away from the impact site. McGregor et al. [70] suggested a couple of possibilities for the giant rings; that they were either a sliding phenomenon or second wave. One other possibility is that these rings are related to the collapse of the outer, invisible shells of the plume which were ejected to much higher altitudes than the visible plume, with correspondingly longer flight times and re-entry velocities. This cause might explain the sizes, locations, and velocities of the rings, but a plausible mechanism for emission is still lacking.

SL-9 Interpretation Summary

The description presented above is designed to provide a conceptual framework for relating the observations to the physical phenomena that were observed, and is not intended to be exhaustive or exclusive. The focus here has been on phenomena that are closely related to the shock physics modeling effort, and that can be identified with features or predictions of those models. The primary intent of this framework is to serve as a descriptive summary of the sequence of events, and to serve as a guide for data interpretation and prioritization of future directions for computational work. Other phenomena associated with the collision, such as the stimulated auroral processes [57],

[72], have less obvious connections to the shock physics models which have not yet been sorted out. More rigorous reviews of the physics of comet entry, fireball growth, and plume collapse, along with a more comprehensive discussion of the related observations, can be found in Noll et al. [36].

PLUME-FORMING COLLISIONS ON EARTH

Plume-forming collisions with Earth had already been investigated theoretically prior to the discovery of SL-9, but the nature of these plumes was somewhat different from those observed on Jupiter. The plumes reviewed by Melosh [28] are dominated by vapor released from an impact with the ground. At the point of impact, strong shock waves are driven into the target and back into the impactor, generating a volume of material at high temperature and pressure that vaporizes upon expansion. As the resulting cloud of vapor is ejected, it sweeps aside the ambient atmosphere and forms a strong blast wave that propagates outward and upward. For small impacts, when the vapor cloud reaches pressure equilibrium with the surrounding atmosphere, its radius is less that of the atmospheric scale height, and it rises buoyantly like a nuclear fireball. Above a threshold energy of about 150 megatons (corresponding to a 3 km diameter crater, and recurring once every several thousand years) the radius of the vapor cloud exceeds the scale height, and the expanding fireball blows out the top of the atmosphere and goes ballistic. One result of such a plume might be the formation of tektite strewn fields as entrained melt quenches to glass and returns to Earth thousands of kilometers away. At even larger scales, such as the Cretaceous/Tertiary extinction event, so much material can be ejected by this mechanism that it can be entrained in the stratosphere and distributed globally. The density of atmospheric debris can be so high that it reduces light levels at Earth's surface, resulting in global cooling [37]. Another serious consequence of the solids ejected with the plume is that when material re-enters the atmosphere it reaches high enough temperatures over a large enough area that wildfires can be ignited by radiative coupling to the surface [29], [50]. Large-scale plumes may also blow off massive quantities of atmosphere, resulting in a net reduction of air, and long-term atmospheric erosion [30].

The SL-9 plumes are fundamentally different, because Jupiter has no surface from which solid material can be shocked to form a dense vapor cloud. Instead, the kinetic energy of the projectile is deposited in an atmospheric wake, which then explodes downward, outward, and upward to form the plume. Shoemaker-Levy 9 is therefore a better analogue to terrestrial impactors with kinetic energies of less than 50 megatons or so, that deposit their energy into the atmosphere and do not reach the ground. Figure 10 makes a direct comparison between the Crawford et al. [14] 3D fireball simulation

and an eyewitness artist's depiction of the February 12, 1947 Sikhote-Alin fireball in Siberia, suggesting that the physics of atmospheric entry and plume generation is similar over many orders of magnitude in the scale of impactor kinetic energy and physical size. The Sikhote-Alin impact energy was 10–20 kilotons [33], whereas the simulated fireball is from a 6 million megaton impact event, nearly a billion times more energetic. The simulation image shows the explosion 50 seconds after the impact of a 3 km diameter fragment on Jupiter. The illustration of the Siberian event, commemorated on a tenth-anniversary Soviet postage stamp, was recorded on canvas by artist P.I. Medvedev. According to most popular accounts, the artist was an eyewitness who recorded his observation immediately after the fall.[1] If the feature depicted by Medvedev represents the debris in the entry column and rising incipient plume, then its resemblance to the Jovian event implies that
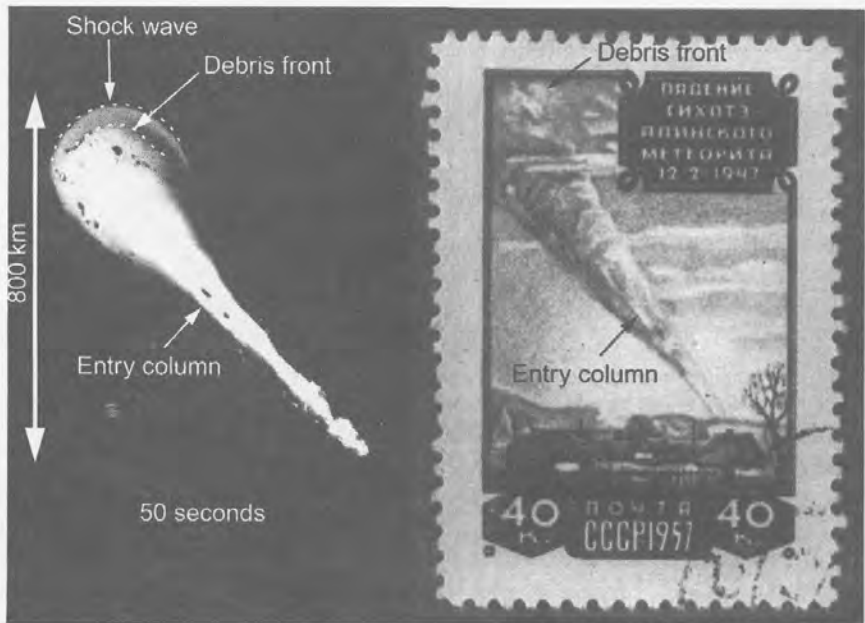

FIGURE 10. Comparison of (a) 3D simulation of impact of 3 km diameter fragment on Jupiter, 50 seconds after entry (from [14]) with (b) artist's depiction of 1947 Sikhote-Alin impact.

---

[1]In part because of publicity associated with this year's fiftieth anniversary of Sikhote-Alin, some doubts have surfaced about this account of the origin of the Medvedev painting, which has been called the "*Mona Lisa* of meteoritical science " [71]. There is now evidence for at least three versions of the painting, and some speculation that the original version was painted with the plume oriented in the wrong direction. Further investigations, however, have demonstrated that the plume was oriented properly (from upper left to lower right) in the original painting, which is actively being sought (O.R. Norton, personal communication).

atmospheric impact explosions behave similarly over many orders of magnitude. The following subsections summarize work in progress to assess the implications of plume-forming collisions on Earth as a hazard to satellites, a collective phenomenon from bolide swarms, a model for the Tunguska explosion, and a mechanism for enhancing transport of material to the upper atmosphere.

Plume-related Satellite Hazards

The simulations and observations of the impact of SL-9 raise some issues that relate to the impact threat to Earth, demonstrating that ballistic impact fireballs and plumes are ejected to very high altitudes, and that explosive expansion of shocked atmosphere along the entry column is highly directional and poorly modeled by point explosions. These observations lead to the suggestion that satellites in low-Earth orbit (LEO) may be vulnerable to ejection of material into their environment by an impact into the atmosphere. Because of the high orbital velocities of these satellites (about 7 km/sec), even a very low-density plume ejected into their path would be catastrophic. For a vapor plume, a satellite/plume interaction would be similar to an atmospheric reentry. At best, an interaction with a very low-density plume would cause a change in the attitude and orbit of the satellite. A worse outcome would result from a higher-density plume, which could cause premature reentry or otherwise destroy the satellite. For a plume containing particles of condensation, like those generated by SL-9, the interaction would involve numerous hypervelocity impacts similar to those occasionally experienced with space debris and micrometeorites. This would most likely end the life of the satellite.

To test this idea, we have performed preliminary 2D simulations of the plume generated by a 34 m diameter stone (density = 3 g/cm^3) impacting at 20 km/sec with vertical incidence. The kinetic energy of the impactor is equivalent to an explosive yield of 3 megatons of TNT, and the expected frequency of such an event is about once per century [31]. The simulation was performed using the same methods as our SL-9 simulations, inserting an appropriate impact energy deposition curve into a gravitationally-stabilized, stratified Earth atmosphere, using the 1976 U.S. Standard Atmosphere (NOAA, NASA, USAF, Washington D.C., 1976) density profile. The energy deposition curve was calculated using the model of Crawford [14] which implies near-negligible radiative ablation for objects greater than about 10 m in diameter (as required by momentum conservation) and hydrodynamic deformation governed by long-wavelength Kelvin-Helmholtz instability. This model has been calibrated with results of entry simulations using CTH. The energy was inserted as 100 discrete energy sources with appropriate magnitudes along the axis of symmetry from 120 km to the surface. The individual

"point charges" were set off sequentially, beginning at the top, and initiating downward with the velocity of the projectile, accounting for its deceleration as it descends into the atmosphere. This method of energy insertion effectively simulates the entry column as a line charge of varying energy density.

(a) 3 MT impact source produces high velocity "ballistic fireball"

Typical satellite orbital altitudes

300 km above surface

← 200 km →

3.3 km/s

3.6 km/s

4.1 km/s

4.3 km/s

3.3 km/s

| 40 | 50 | 60 | 80 | 100 |

Time after impact (seconds)

(b) 3 MT explosion source produces low velocity "buoyant fireball"

420 m/s   400 m/s   360 m/s   310 m/s   225 m/s

100 km

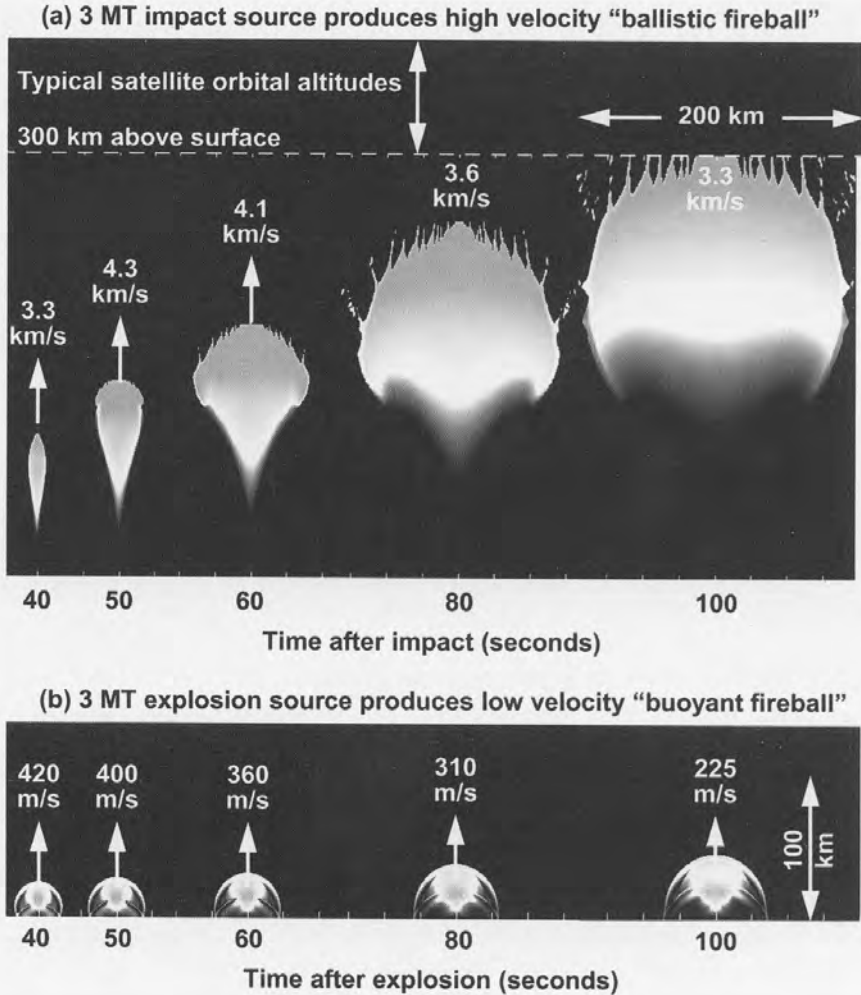| 40 | 50 | 60 | 80 | 100 |

Time after explosion (seconds)

FIGURE 11. Comparison on the same scale of evolution of (a) ballistic fireball generated by 3 megaton impact to (b) buoyant fireball generated by a 3 megaton explosion at same altitude of maximum energy deposition (7 km). Shading indicates velocity magnitude of the air as indicated in the text.

A time sequence showing the results of the simulation is given in Fig. 11. The shading indicates material velocity magnitudes, ranging from 100 m/sec to 3 km/sec. Immediately after entry, the meteoroid has deposited its energy in a long column, with a sharp peak in the energy deposition curve at an altitude of 7 km. The column begins to expand explosively the instant that energy is deposited in the column, so by the time the object reaches the bottom, the top of the column has had time to expand and accelerate upwards. When the main fireball begins to develop lower down, it expands most easily up along the low-density, high-sound-speed column that is already moving upward. In this way, much of its mass is accelerated and launched into space as a "ballistic fireball." At about 100 seconds after atmospheric entry, the top of the plume (as defined by the 120 km density contour) has reached an altitude of nearly 300 km, and is still moving upward at a velocity of about 3 km/sec (the "fingers" protruding from the top of the plume are an artifact of instabilities resulting from the relatively low resolution used for this simulation). Ballistic extrapolation indicates a peak plume height at about 800 km, putting it across the path of many satellites in LEO. The plume will have a "hang time" greater than 10 minutes; during this interval it will obstruct any satellite passing overhead. Furthermore, it will continue to expand radially during this time to cover a region thousands of kilometers in diameter. Observations and simulations of the plume collapse on Jupiter imply that the atmospheric density contours in the region of collapse will remain elevated for a much longer period of time, posing a further risk to satellites entering the area.
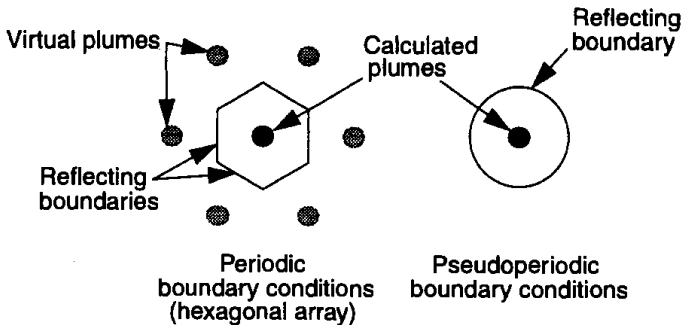

FIGURE 12. Diagrammatic explanation of 2D pseudoperiodic computational scheme (plan view).
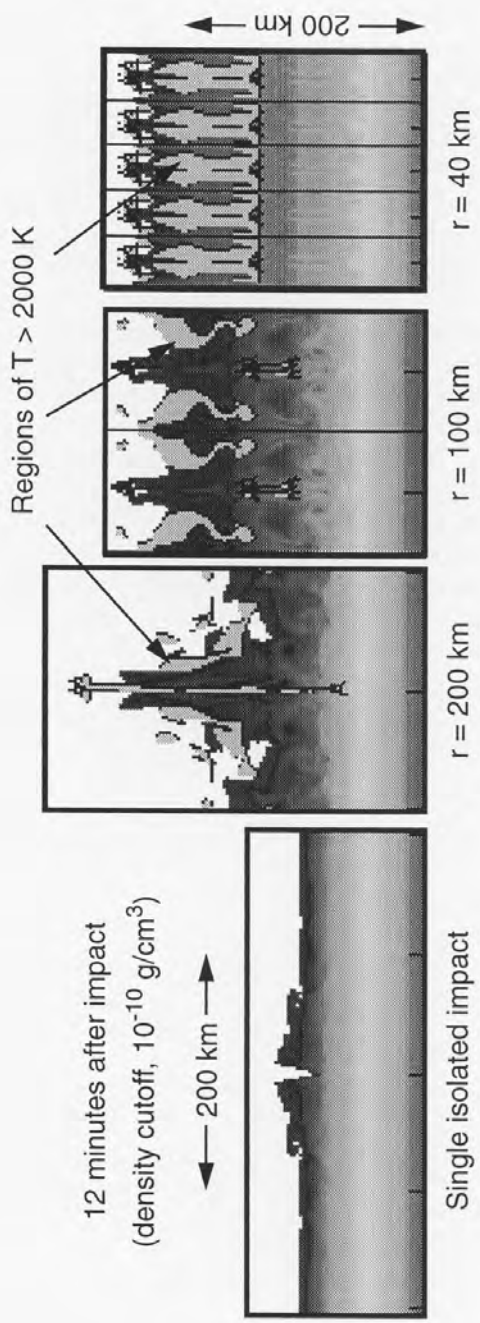
FIGURE 13. Plumes from clusters of 3 MT impacts, showing density bands of collapsed plume at 12 minutes after impact, with regions where temperature exceeds 2000 K; r is the interaction distance between neighboring impacts.
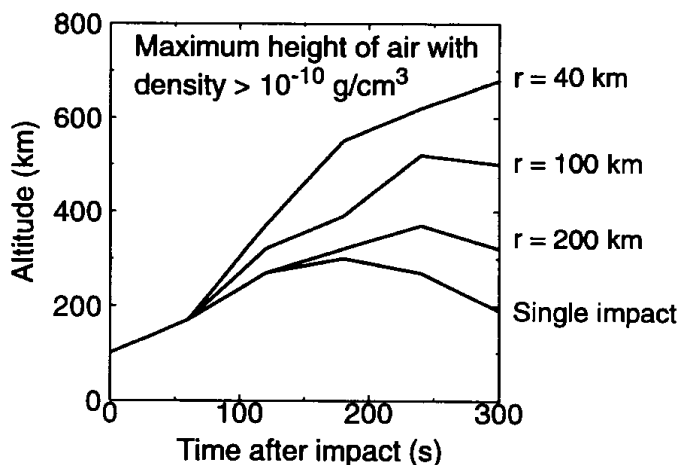
FIGURE 14. Plot of maximum height of 10–10 g/cm^3 isodensity surface as a function of time, for various plume separation distances resulting from bolide swarm.

Plume Clusters

We have also simulated the interaction of atmospheric impact plumes generated by an array of simultaneous impact events on Earth. Wasson [47] has suggested that atmospheric deposition of energy from a disrupted comet or asteroid may have led to the formation of layered (Muong-Nong) tektites by a process of radiative coupling, so there is possible evidence in the geologic record for such atmospheric plume phenomena. In addition, NEO threat pulverization strategies such as those proposed by Wood et al. [49], could potentially produce broad clusters of closely spaced impactors if there was insufficient time to disperse the fragments. As a first step toward modeling an array of plumes, we approximated a swarm of equally-spaced impacts by performing an axisymmetric simulation in a cylinder with reflecting boundary conditions. The diameter of the cylinder is roughly the distance between plumes in a hexagonal array with periodic boundary conditions, so these boundary conditions can be considered "pseudoperiodic" (Fig. 12). In this highly simplified geometry, the lateral extent of the cluster is infinite, but for a 1000 km cluster the effects of the edge will not reach the center of the collective plume until after it has collapsed.
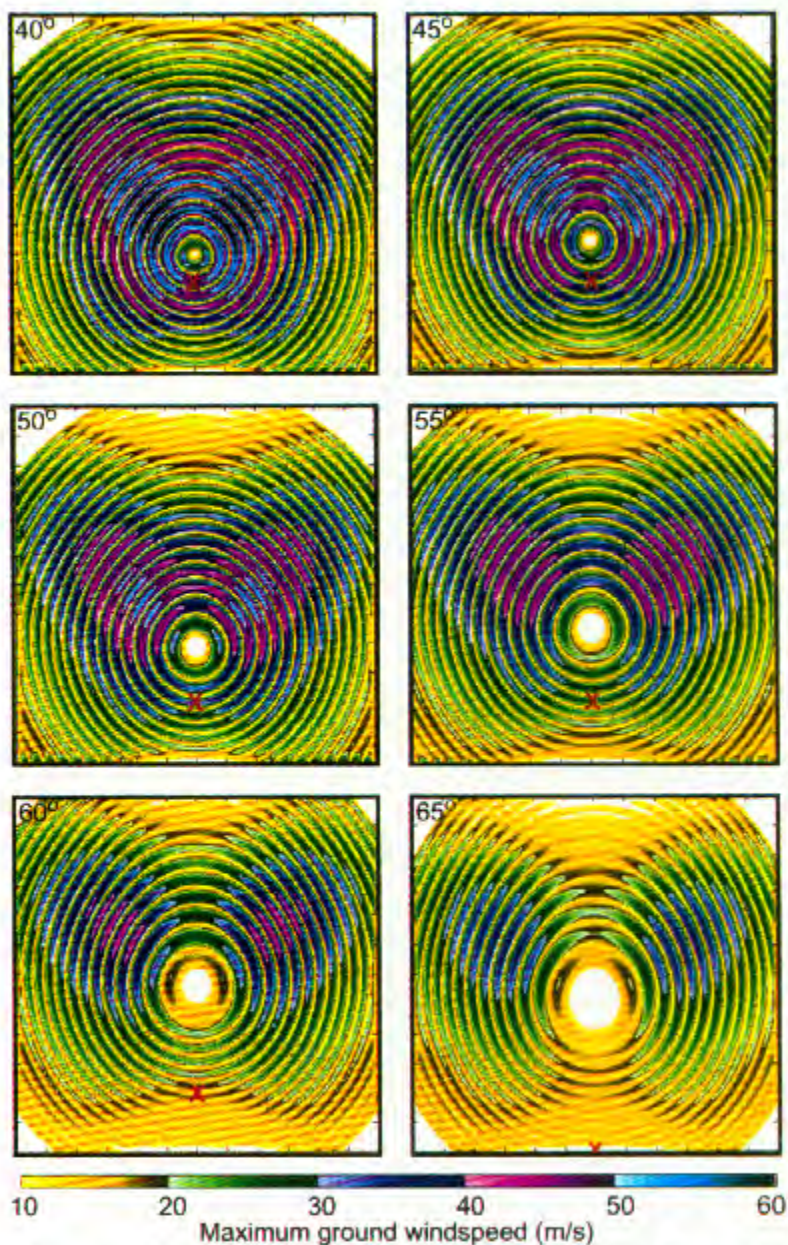
FIGURE 15. Plan view of peak surface windspeeds determined from 3D simulations of 12 megaton plume-forming collisions. Concentric zones show the magnitude of radially-directed winds at 5-second intervals. Various oblique entry angles (given from zenith) were simulated.
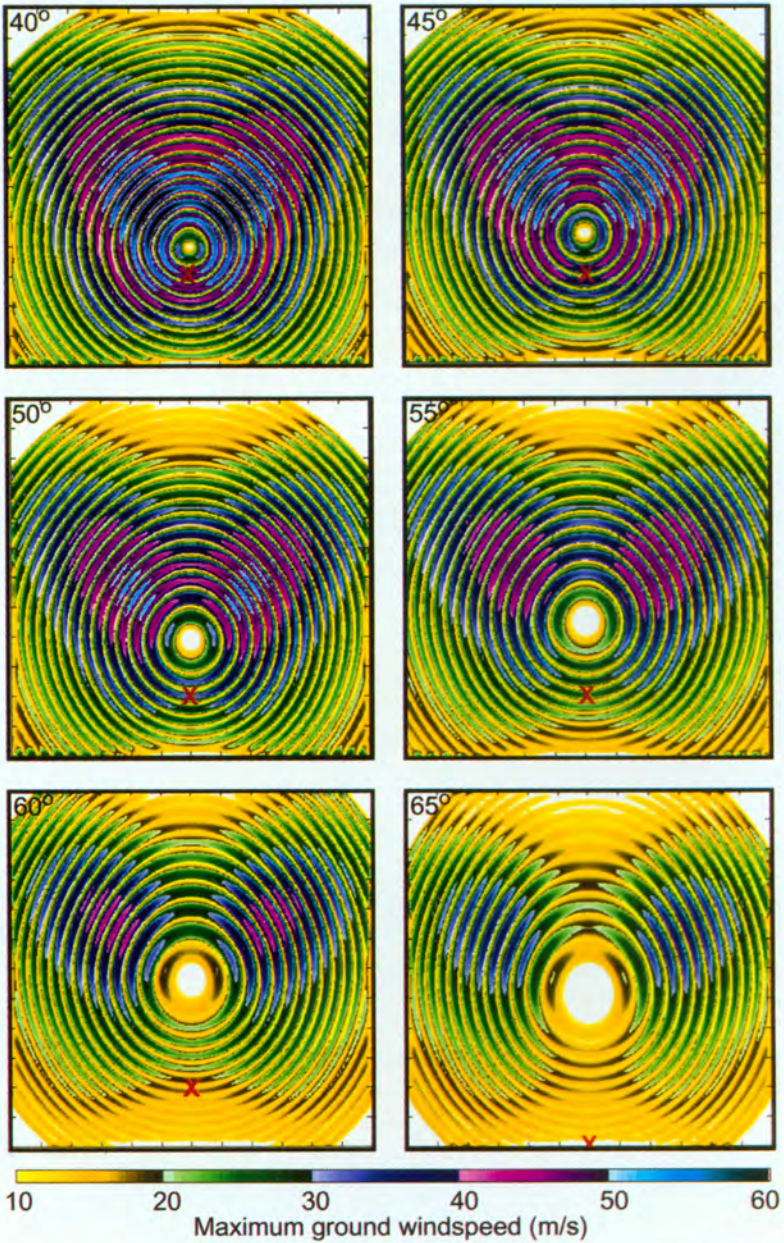
FIGURE 15. Plan view of peak surface windspeeds determined from 3D simulations of 12 megaton plume-forming collisions. Concentric zones show the magnitude of radially-directed winds at 5-second intervals. Various oblique entry angles (given from zenith) were simulated.
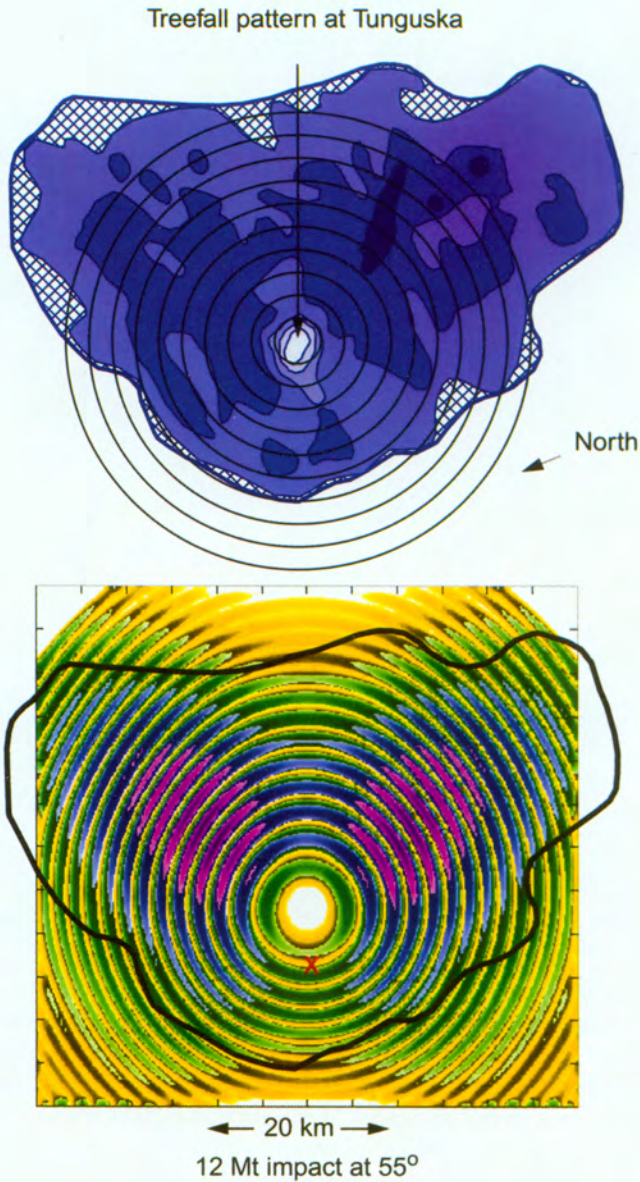
FIGURE 16. Comparison of butterfly-shaped treefall pattern at Tunguska [17] to map of peak surface windspeeds calculated from the collision of a 12 megaton object entering the atmosphere at an oblique angle, 55° from the zenith.
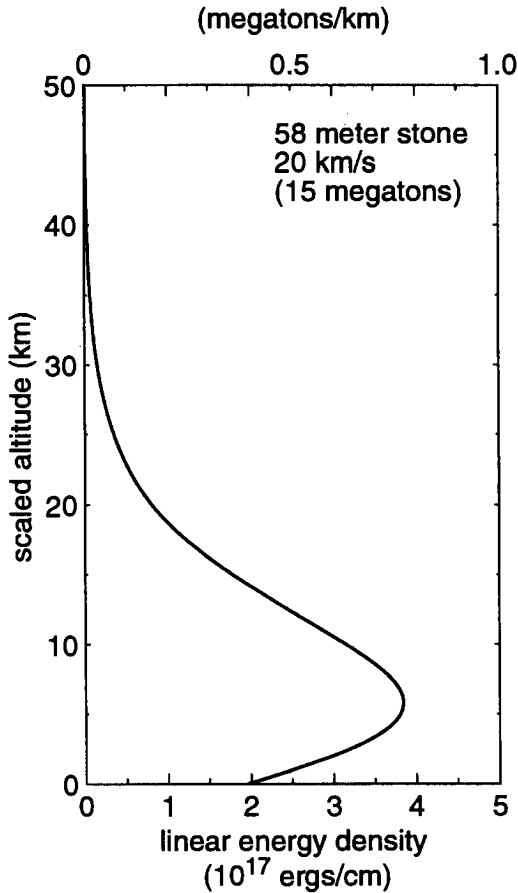
FIGURE 17. Energy deposition curve from a 15 megaton impact at a 45° entry angle, used to generate the plume depicted in Figs. 18–19.

We simulated a plume from the impact of a 20 km/sec, 34 meter-diameter asteroid (kinetic energy of 3 megatons) at vertical incidence, and compared its evolution and collapse to interacting plumes from arrays of impacts with near-neighbor separation distances of 40, 100, and 200 km. As expected, the closer-packed arrays lead to denser plumes that reach higher altitudes and generate higher temperatures within denser air upon collapse. The time steps at 12 minutes after impact of each simulation are shown in Fig. 13, where the shading is proportional to log(density) with a cutoff density of 10–10 g/cm^3. The regions where the temperature is greater that 2,000 K are also shown. Figure 17 provides maximum altitude as a function of time of air

with density greater than 10^{-10} g/cm^3. Because more mass is ejected per unit area for the tighter cluster, the density of the plume is higher and much more atmospheric mass is heated upon its collapse. The energy transport in these simulations neglects radiation, so the actual late-time atmospheric temperatures may be lower. To fully assess the effects of radiative energy coupling to the ground will require a simulation that includes detailed opacity calculations.

Tunguska

The 1908 Tunguska explosion was almost certainly a plume-forming impact. Estimates for the magnitude of the event vary by a wide margin, but by virtually all accounts the yield was significantly more than 3 megatons, implying that the scale of the resulting plume was at least comparable to that shown in Figure 11. The similarity between the terrestrial and Jovian impact plume simulations suggests that phenomena associated with the Tunguska event should be re-examined in the context of these models, and that estimates for its energy should be revisited. Our model incorporates most of the physics that was first applied to the Tunguska event by Chyba et al. [56], but in addition couples the momentum and energy of the impacting body to the atmosphere along the entire entry path, leading to the extended "line explosion" that results in plume formation as well as enhanced momentum and energy coupling to the ground.

For reasons of practicality, most of the published models for Tunguska have assumed that the explosion was essentially a point source, and the most widely quoted yield estimates are based on this approximation. These calculations made use of seismic records, barograms, and measurements of fallen trees, and are calibrated with nuclear airburst data (see Sekanina [73] for a review of the relevant data). In all cases, however, the point source approximation coupled with other simplifications may have led to serious overestimates of the yield of the Tunguska explosion. One of the most solidly accepted values for the energy of Tunguska is that of Ben-Menahem [54], who analyzed old records from four seismic stations and compared them to modern seismograms recorded during Soviet and Chinese atmospheric nuclear tests. He concluded that the ground motion resulted from a vertical point impulse of 7×10^{18} dyn sec, which would be generated by a point explosion of about 12.5 megatons at an altitude of 8.5 km. However, our simulations of a 3 megaton event reveal that within the first minute of impact, the upward-directed momentum associated with the atmospheric plume has reached 7×10^{18} dyn sec, requiring that a reaction impulse sufficient to generate the observed seismic records has been coupled to the ground. This implies that, from a seismic standpoint, a 3 megaton plume-forming event gives the appearance of being a much larger point source explosion. Likewise, the strong momentum anisotropy associated with plume formation was not taken into consideration for estimates based on atmospheric waves [65], [54].

There are many discrepancies among the various estimates based on tree-fall [78], [77], [80], [54], [73], which in all cases make comparisons between the damage at Tunguska and the criteria for blast damage to forests established by the nuclear weapons effects literature, and range from "a few megatons" up to 50 megatons. This is the most reasonable approach, but it is important to recognize the limitations associated with using the weapons tables, which apply to living coniferous forests [62] and implicitly assume flat topography. There is cause for skepticism of these yield estimates, because it is clear from the photographs of Krinov [68], that slopes of 15–20 degrees and greater are typical of the terrain around the impact site. A 15 degree upslope results in a secondary Mach stem (in addition to the one that forms from the flat-ground reflection) that increases the dynamic pressure by a factor of 3 for weak shock, so the topography at Tunguska would naturally lead to concentrations of blast wave energy far beyond the distance that would be calculated assuming flat terrain. One must assume that the most distant fallen trees were in such areas, so a yield estimate based on the extent of treefall would be too high. Krinov [68] indeed described a treefall pattern that was dependent on local topography, and in all his photographs showing the forest devastation, there are many trees that remain standing.

Another reason to be skeptical of treefall-based yield estimates is that none of them take into account the pre-impact condition of the Siberian forest at the site of the explosion. One result of a 1961 expedition to the site [60], was that "the region of the forest flattened in 1908 was not one of homogeneous primeval intact taiga," and that according to an expert from the Forestry and Lumber Institute of the Siberian Branch of the Academy of Sciences, "... the region of meteorite impact in 1908 was basically a fire-devastated area ... a partly flattened dead and rotting forest was standing in this area ... ." Because of this observation, Florenskiy [60] issued the apparently unheeded advice that "... an estimate of the force of the shock wave that is based on the number of flattened trees must necessarily take into consideration the condition of the forest at that time." Fortunately, he provided some of the data required for that task, in the form of dynamometry measurements of the force required to fell trees of various sizes and conditions. A key graph in his paper shows that the felling moment of trees from a dead timber stand of 1908 are about one third that for living trees of the same diameter. Even after accounting for lower wind resistance of dead timber, one would expect the forest at Tunguska to be blown down by a significantly smaller explosion than would be required to destroy the same area of a healthy forest. Dynamic pressure scales as the square of wind speed, so the peak wind speeds for flattening the forest could be reduced by as much a 40% from the values previously assumed.

To provide some quantitative estimates of wind speed at ground level, we performed a series of 3D simulations, with 500 meter resolution, for various

entry angles of a 12 megaton impact. The results (Fig. 15) show the charac-
teristic butterfly pattern that has been reproduced experimentally by Zotkin
and Tsikulin [78], and analytically by Korobeinicov et al. [67]. The peak
wind speeds immediately behind the shock front are plotted at 5-second in-
tervals. For comparison, the peak wind speed is 40 m/sec at a distance of 23
km from a 12 megaton point explosion at its optimum height of burst. Ac-
cording to Glasstone [62], this is the threshold for severe treefall (defined as
90% blow down of a conifer forest) by aerodynamic drag pressure from a 12
megaton explosion. Similarly, Glasstone's radius to moderate damage (30%
blow down) for a 12 megaton air burst is 29 km, where the maximum wind
speed is about 30 m/sec. If the requisite wind speeds can be reduced by 40%,
as suggested by the dynamometer data Florenskiy [60], then the required
point source energy (at optimum height) to achieve the same radius for se-
vere damage is about 3.5 megatons [62].

Since the maximum wind speed contours are dependent on entry angle,
the calculated butterfly patterns can be used to estimate the angle by com-
paring them to the treefall data of Fast [17]. These data are presented in Fig-
ure 16, where the contours represent the average scatter in the deviation of
the angle of uprooted trees from the radial direction, a parameter that pre-
sumably depends on aerodynamic pressure. The best agreement is for a ze-
nith angle of about 55°, which is very close to the 60° angle favored by
Zotkin and Tsikulin [79]. The contour map of Fast [17] shows a high degree
of bilateral symmetry, but there are also significant deviations that are prob-
ably related both to topography and pre-impact inhomogeneities in the taiga.
A useful next step would be to perform high resolution 3D simulations of im-
pacts, using actual topography data from Tunguska.

One of the most unusual phenomena associated with Tunguska was the
bright sky over an extensive region of Europe and Asia for several consecu-
tive nights after the explosion. Many of the early papers, especially those by
Soviet researchers [59], argue that the Eurasian bright nights were evidence
for a cometary tail that was directed southwestward from the point of the im-
pact, giving rise to the observed geographic distribution which extended
southward about two thousand kilometers, and westward through Europe to
the Atlantic Ocean. More recently, investigators have attempted to explain
the bright sky in terms of noctilucent clouds made up of water ice and dust
generated by the impact and transported westward by high-altitude horizon-
tal winds. Noctilucent clouds reside in the mesosphere, at altitudes ranging
from 75 to 90 km, and are most visible at high latitudes during midsummer
when they are in direct sunlight all night long on account of low solar dec-
linations. The Tunguska explosion took place at 60° north, and only 9 days
after the summer solstice. Turco et al. [75] suggest that the clouds were con-
densed primarily from the vapor ablated at very high altitude from the enter-
ing meteor. However, this model requires an extremely low density meteor

of less than 0.01 gm/cm^3 in order to deposit sufficient mass (about 3×10^9 g) above 50 km. Turco et al. [75] point out that deposition above this altitude would be necessary for the cloud to have been transported westward rapidly enough by easterly winds to have been visible 6000 km away, in England, within 12 hours. Chyba et al. [56] were able to find a mechanism capable of transporting as much as 3×10^{12} g of water vapor aloft, reasoning that atmospheric humidity could be lifted by a buoyant fireball that rose to about 40 km from the 15 megaton terminal explosion.

We agree that the light nights were caused by noctilucent clouds made up of water and dust generated by the impact, but the recognition that Tunguska was a plume-forming event simplifies the explanation significantly. The easiest argument is made simply by analogy to the aftermath of the impact on Jupiter. At time (e) in Figs. 1 and 3, the geometry of the collapsed plume from SL-9 can be seen to be on the nighttime side of the terminator, yet parts of it are at high enough altitude to be illuminated by the Sun. The HST image taken at 7:51 UT on July 18, 1994 of the collapsed plume from impact G is shown in Fig. 6(b). which reveals a sunlit cloud extending above and beyond Jupiter's terminator. This feature is, by definition, a noctilucent cloud.

We chose to model the formation of the plume at Tunguska by depositing the energy of a 58 m diameter stony asteroid (3 g/cm^3) striking the atmosphere at 20 km/sec at a 45° entry angle, using the model of Crawford [12]. The energy deposition curve is shown in Fig. 17, and represents a total energy of 15 megatons. These were 2D axisymmetric simulations, with the atmosphere scaled by a factor of 1.414 to accommodate the actual density gradient encountered by the oblique impact. The resulting plume, 100 seconds after impact, is shown in Fig. 18, with tracer particles showing the ballistic trajectories of air packets derived from altitudes of 350 m, 1.4 km, 7.1 km, and 90 km. Material within a cylinder nearly 1 km in diameter has been accelerated to sufficient speed to escape the mesosphere, and it is this mixture of vaporized meteor and tropospheric air that we would expect to condense in the upper atmosphere to form the noctilucent clouds observed across Europe. We can approximate the mass of entrained water by estimating the volume of ejected air and assuming a humid troposphere as was done by Chyba et al. [56]. Our result is that about 10^{11} g of water collapses with the plume on top of the mesosphere, along with virtually the entire 3×10^{11} g mass of the vaporized meteor. Ballistic extrapolation of the plume reveals that, in the absence of significant atmospheric dissipation, the ejected material extended more than 2000 km from the impact site within 15 minutes (Fig. 19). If the bolide arrived from the southeast, as most evidence indicates, then the plume was ejected back in that direction, and may have reentered the atmosphere as far away as Lake Baikal. The lateral extent of this collapsed plume is fully consistent with that of the noctilucent cloud, extending as far south as 45°N latitude.

All the modeling on which the above reinterpretations are based is pre-
liminary, and it is too early to make strong quantitative conclusions. Many
of the simulations were 2D, and the 3D simulations were probably insuffi-
ciently resolved. Radiative transport was not included, and significant work
is required to develop a complete entry model that accounts for all the phys-
ics. Nevertheless, the formation of atmospheric plumes by deposition of an
energy profile that resembles Fig.17 is a highly robust result. Plume forma-
tion does not appear to be strongly dependent upon the details of the assump-
tions, leaving little doubt that Tunguska-class impacts are plume-forming
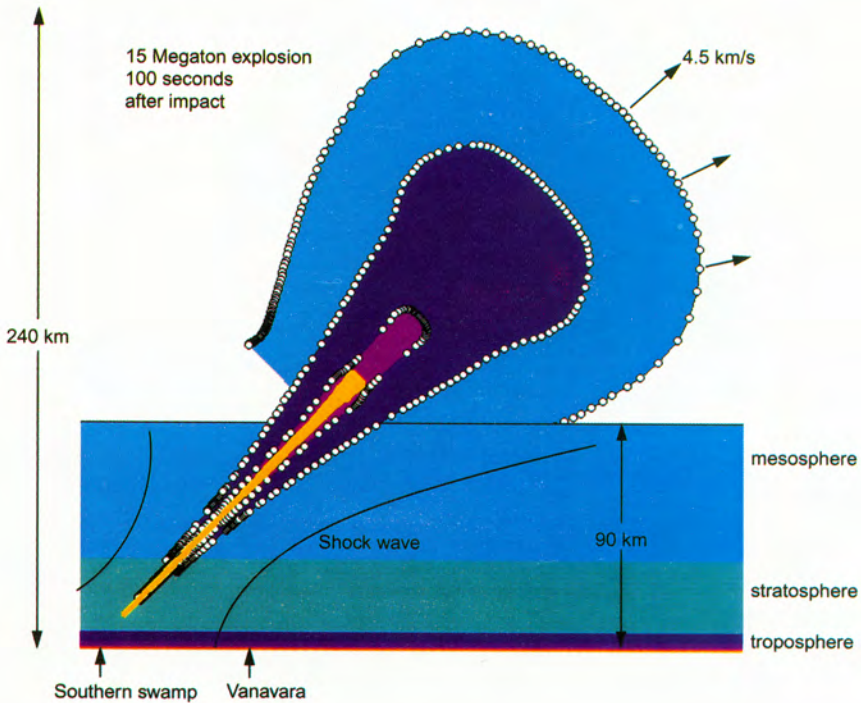events.

FIGURE 18. Anatomy of a 15 megaton plume, 100 seconds after impact. Material
within all but the outermost shell has been ejected from within the troposphere, and con-
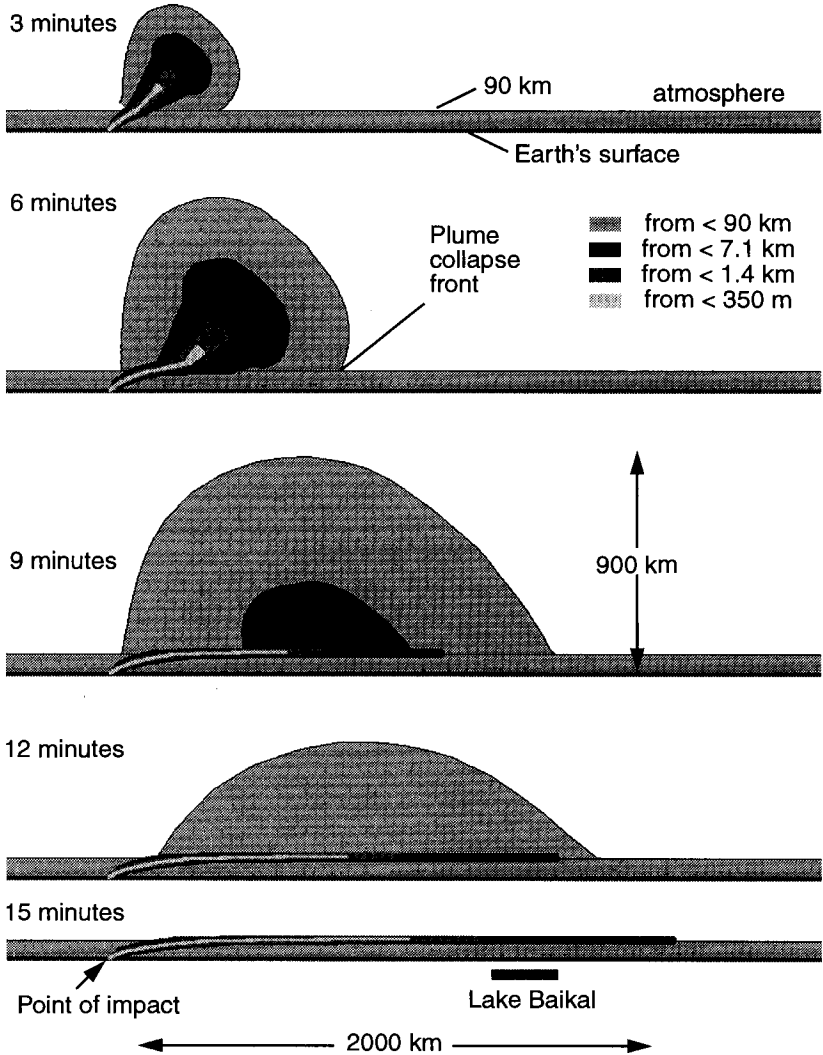tains the mass of the impactor, as well as water from the humid lower atmosphere.

FIGURE 19. Growth and collapse of the 15 megaton plume over a period of 15 minutes, showing that tropospheric water and meteoritic debris can be distributed over distances of thousands of kilometers at mesospheric altitudes.

Observational Validation

The impact of SL-9 underscores the importance of observational valida-tion of impact modeling. It is probably not realistic to expect another oppor-tunity to watch a comet collide with Jupiter, an event that only happens once in a period ranging from 200 to 10,000 years [41]. A more reasonable plan would be to attempt to gather as much information as possible about the smaller atmospheric impacts that are continuously taking place on Earth. If the physics of atmospheric entry and plume formation is indeed similar at scales that are different by more than 9 orders of magnitude, then careful, quantitative measurements of impacts that take place at intervals of a year or less would help give entry and impact models the degree of validity neces-sary to allow their use as a basis for hazard assessment for the smallest Earth-threatening impacts. To accomplish this task, we recommend a coor-dinated campaign based on a combination of satellite sensors and Earth-based observations. Infrared and visible-light sensors on satellites operated by the U.S. Department of Defense have already detected over a hundred events [44], including the February 1, 1994 bolide over the South Pacific with an estimated energy of 40–70 kilotons [32]. Microbarograph records are particularly useful in characterizing the explosive yield of large impact events, and have recorded an explosion as large as 1.1 megatons for the Au-gust 3, 1963 bolide (possibly in the plume-forming class) over the ocean south of Africa [38]. Other sources of data that can be used to validate the simulations are photographic and video images (e.g., [8], [5]), infrasound [38], and seismic data.

There is one major drawback in all the above methods as they have been used to date: the events they observed were not predicted in advance. There-fore, the instrumentation was operated in "open shutter" mode, or set to trig-ger off of the event, or relied on serendipity. By contrast, the impact of SL-9 was predicted a year in advance, and observing plans were carefully as-sembled well in advance of the event, resulting in the collection of vast amounts of high-quality data. We suggest a similar strategy would be most useful for validation of Earth impact models. A ground-based search system capable of providing short notice of an impact in the 100 kiloton range would mean that the approaching object could be characterized before im-pact. Moreover, arrays of sensors, cameras, and satellite observing plans to be quickly put in place so that data from the event could be captured and used to provide quantitative validation.

The enhancement in modeling sophistication brought about by further in-creases in high performance computing capabilities will allow impact mod-els to continue to be advanced and refined, which should reduce the uncertainties and improve the risk assessments. However, until the next large impact takes place, the data from SL-9 will be the only true reality check for models of collisions with planetary atmospheres.

REFERENCES

1. AHRENS, T.J., T. TAKATA, J.D. O'KEEFE, & , G.S. ORTON. 1994. Radiative signatures from impact of Comet Shoemaker-Levy 9 on Jupiter. Geophys. Res. Lett. **21:** (14) 1551–1553.
2. BOSLOUGH, M.B., D.A. CRAWFORD, A.C. ROBINSON, & T.G. TRUCANO. 1994. Mass and penetration depth of Shoemaker-Levy 9 fragments from time-resolved photometry. Geophys. Res. Lett. **21:** (14) 1555–1558.
3. BOSLOUGH, M.B., D.A. CRAWFORD, A.C. ROBINSON, & T.G. TRUCANO. 1994. Watching for fireballs on Jupiter. Eos. **75:** 305–310.
4. BOSLOUGH, M.B., D.A. CRAWFORD, T.G. TRUCANO, & A.C. ROBINSON. 1995. Numerical modeling of Shoemaker-Levy 9 impacts as a framework for interpreting observations. Geophys. Res. Lett. **22:** (13) 1821–1824.
5. BROWN, P., Z. CEPLECHA, R.L. HAWKES, G. WETHERILL, M. BEECH, & K. MOSSMAN. 1994. The orbit and atmospheric trajectory of the Peekskill meteorite from video records. Nature. **367:** 624–626.
6. CARLSON, R.W., P.R. WEISSMAN, M. SEGURA, & THE NIMS SCIENCE TEAM. 1995. Galileo infrared observations of the Shoemaker-Levy 9 G impact fireball: A preliminary report. Geophys. Res. Lett. **22:** (12) 1557–1560.
7. CARLSON, R.W., P. DROSSART, TH. ENCRENAZ, P.R. WEISSMAN, J. HUI, & M. SEGURA. 1997. Temperature, size and energy of the Shoemaker-Levy 9 G-impact fireball. Icarus. In press.
8. CEPLECHA, Z. 1994. Earth-grazing daylight fireball of August 10, 1972. Astron. Astrophys. **283:** 287–288.
9. CHAPMAN, C.R., W.J. MERLINE, K. KLAASEN, & THE GALILEO IMAGING TEAM. 1995. Preliminary results of Galileo direct imaging of S-L 9 impacts. Geophys. Res. Lett. **22:** 1561–1564.
10. CHAPMAN, C.R. 1996. Galileo observations of the impacts. *In* The Collision of Comet Shoemaker-Levy 9 and Jupiter, K.S. Noll, H.A. Weaver, P.D. Feldman, Eds.: 121–132. Cambridge University Press.
11. CHODAS, P.K. & D.K. YEOMANS. 1996. The orbital motion and impact circumstances of comet Shoemaker-Levy 9. *In* The Collision of Comet Shoemaker-Levy 9 and Jupiter, K.S. Noll, H.A. Weaver, & P.D. Feldman, Eds.: 1–30. Cambridge University Press.
12. CRAWFORD, D.A. 1996. Models of fragment penetration and fireball evolution. *In* The Collision of Comet Shoemaker-Levy 9 and Jupiter, K.S. Noll, H.A. Weaver, & P.D. Feldman, Eds.: 133–156. Cambridge University Press.
13. CRAWFORD, D.A., M.B. BOSLOUGH, T.G. TRUCANO, & A.C. ROBINSON. 1994. The impact of comet Shoemaker-Levy 9 on Jupiter. Shock Waves. **4:** (1) 47–50.
14. CRAWFORD, D.A., M.B. BOSLOUGH, A.C. ROBINSON, & T.G. TRUCANO. 1995. Dependence of Shoemaker-Levy 9 impact fireball evolution on fragment size and mass. Lunar and Planetary Science XXVI: 291–292.
15. CRAWFORD, D.A., M.B. BOSLOUGH, T.G. TRUCANO, & A.C. ROBINSON. 1995. The impact of periodic comet Shoemaker-Levy 9 on Jupiter. Int. J. Impact. Engng. **17:** 253–262.
16. DEMING, D. & J. HARRINGTON. 1995. Unpublished presentation. IAU Colloquium 156, Baltimore, MD.
17. FAST, V.G. 1967. Statisticheskij analiz parametrov Tungusskogo vyvala. *In* Problema Tungusskogo Meteorita, Part 2: 40–61. Izdatelstvo Tomskogo Universiteta, Tomsk.
18. GRAHAM, J.R., I. DE PATER, J.G. JERNIGAN, M.C. LIU, & M.E. BROWN. 1995. The fragment R collision: W. M. Keck telescope observations of SL-9. Science. **267:** 1320–1323.

19. HAMMEL, H.B., R.F. BEEBE, A.P. INGERSOLL, ET AL. 1995. HST Imaging of atmospheric phenomena created by the impact of Comet Shoemaker-Levy 9. Science. **267:** 1288–1296.

20. HORD, C.W., W.R. PRYOR, A.I.F. STEWART, ET AL. 1995. Direct observations of the comet Shoemaker-Levy 9 fragment G impact by Galileo UVS. Geophys. Res. Lett. **22:** (13) 1565–1568.

21. KERLEY, G.I. 1991. User's Manual for PANDA II: A Computer Code for Calculating Equations of State: SAND88-2291. Sandia National Laboratories.

22. LIVENGOOD, T.A., G. BJORAKER, T. KOSTIUK, ET AL. 1994. Bull. Am. Astr. Soc. **26:** supplement.

23. MAC LOW, M.-M. 1996. Entry and fireball models vs. observations: What have we learned? *In* The Collision of Comet Shoemaker-Levy 9 and Jupiter, K.S. Noll, H.A. Weaver, & P.D. Feldman, Eds.: 157–182. Cambridge University Press.

24. MAILLARD, J.-P., P. DROSSART, B. BEZARD, ET AL. 1995. Methane and carbon monoxide infrared emissions observed at the Canada-France-Hawaii telescope during the collision of Comet SL-9 with Jupiter. Geophys. Res. Lett. **22:** (12) 1573–1576.

25. MARTEN, A., D. GAUTIER, M.J. GRIFFEN, ET AL. 1995. The collision of Comet Shoemaker-Levy 9 with Jupiter: Detection and evolution of HCN in the stratosphere of the planet. Geophys. Res. Lett. **22:** (12) 1589–1592.

26. MARTIN, T.Z., G.S. ORTON, L.D. TRAVIS, L.K. TAMPPARI, & I. CLAYPOOL. 1995. Observation of Shoemaker-Levy impacts by the Galileo photopolarimeter radiometer. Science. **268:** 1875–1878.

27. MCGLAUN, J.M., S.L. THOMPSON, & M.G. ELRICK. 1990. CTH: A three-dimensional shock-wave physics code. Int. J. Impact. Engineering. **10:** 351.

28. MELOSH, H.J. 1989. Impact Cratering a Geologic Process. Oxford University press. New York, NY. 245 pp.

29. MELOSH, H.J., N.M. SCHNEIDER, K. ZAHNLE, & D. LATHAM. 1990. Ignition of global wildfires at the Cretaceous/Tertiary boundary. Nature. **343:** 251–254.

30. MELOSH, H.J. 1991. Atmospheric impact processes. Adv. Space Res. **11:**(6) 87–93.

31. MORRISON, D., C.R. CHAPMAN, & P. SLOVIC. 1995. The impact hazard. *In* Hazards Due to Comets and Asteroids, T. Gehrels, Ed.: 59–91. 1995. Univ. Arizona Press, Tucson, Arizonia.

32. NEMCHINOV, I.V. 1994. Assessment of the 1 February 1994 Event. Interim Report 006 to Sandia National Laboratories.

33. NEMCHINOV, I.V. 1995. Analysis of the 12 February 1947 Event. Interim Report 01A to Sandia National Laboratories.

34. NICHOLSON, P.D., ET AL. Palomar Observations of the R Impact of Comet Shoemaker-Levy 9: I. Light Curves," Geophys. Res. Lett., 22(12), 1589-1592, 1995.

35. NICHOLSON, P.D. 1996. Earth-based observations of impact phenomena. *In* The Collision of Comet Shoemaker-Levy 9 and Jupiter, K.S. Noll, H.A. Weaver, & P.D. Feldman, Eds.a; 81–109. Cambridge University Press.

36. NOLL, K.S., H.A. WEAVER, P.D. FELDMAN, EDS. 1996. The Collision of Comet Shoemaker-Levy 9 and Jupiter. Cambridge University Press.

37. O'KEEFE, J.D. & T.J. AHRENS. 1982. The interaction of the Cretaceous/Tertiary Extinction Bolide with the atmosphere, ocean, and solid Earth. *In* Geological Implications of Impacts of Large Asteroids and Comets on the Earth, L.T. Silver & P.H. Schultz, Eds.: pp. 103–120. Geological Soc. of America Special Paper 190, Boulder: Geological Soc. of America.

38. REVELLE, D.O. 1997. Historical detection of atmospheric impacts by large bolides using acoustic-gravity waves. *In* Near-Earth Objects: The United Nations Conference on Near-Earth Objects, New York, April 24–26, 1995. Annals of the New York Academy of Sciences. This *volume*, **822:** 284–302.

39. ROOS-SEROTE, M., A. BARUCCI, J. CROVISIER, P. DROSSART, M. FULCHIGNONI, J. LECACHEUX, & F. ROQUES. 1995. Metallic emission lines during the impacts L and Q1 of Comet P/Shoemaker Levy 9 in Jupiter. Geophys. Res. Lett. **22:** (12) 1621–1624.

40. SHOEMAKER, E.M. 1995. Comet Shoemaker-Levy 9 at Jupiter. Geophys. Res. Lett., **22:** (12) 1555–1556.

41. SHOEMAKER, E.M., P.J. HASSIG, & D.J. RODDY. 1995. Numerical simulations of the Shoemaker-Levy 9 impact plumes and clouds: A progress report. Geophys. Res. Lett. **22:** (13) 1825–1828.

42. STELLINGWERF, R.F., N.M. HOFFMAN, & C.A. WINGATE. 1994. Bull. Am. Astr. Soc. **26:** 880.

43. SWEGLE, J.W. & A.C. ROBINSON. 1989. Acceleration instability in elastic-plastic solid. I. Numerical simulations of plate acceleration. J. Appl. Phys. **66:** 2838.

44. TAGLIAFERRI, E., R. SPALDING, C. JACOBS, P. WORDEN, & A. ERLICH. 1995. Detection of meteoroid impacts by optical sensors in Earth orbit. *In* Hazards Due to Comets and Asteroids, T. Gehrels, Ed.: 199–220. Univ. Arizona Press. Tucson, Arizona.

45. TAKEUCHI, S., H. HASEGAWA, J. WATANABE, ET AL. 1995. Near-IR imaging observations of the cometary impact into Jupiter. Geophys. Res. Lett. **22:** (12) 1581–1584.

46. THOMPSON, S.L. 1989. ANEOS Analytic Equations of State for Shock Physics Codes Input Manual: SAND89-2951. Sandia National Laboratories.

47. WASSON, J.T. 1995. *In* Lunar Planet Sci. XXVI: 1469–1470.

48. WEAVER, H.A., ET AL. 1995. The Hubble Space Telescope (HST) observing campaign on Comet Shoemaker-Levy 9. Science. **267:** 1282–1288.

49. WOOD, L., R. HYDE, M. ISHIKAWA, & E. TELLER. 1995. Cosmic Bombardment V: Threat Object-Dispersing Approaches to Active Planetary Defense, Planetary Defense Conference, LLNL.

50. ZAHNLE, K. 1990. Atmospheric chemistry by large impacts. *In* Global Catastrophes in Earth History, V.L. Krypton & P.D. Ward, Eds.: 271–288, Geological Soc. of America special Paper 247, Boulder: Geological Soc. of America.

51. ZAHNLE, K., & M.-M. Mac Low. 1994. The Collision of Jupiter and Comet Shoemaker-Levy-9. Icarus. **108:** 1–17.

52. ZAHNLE, K. 1996. Dynamics and chemistry of SL9 plumes. *In* The Collision of Comet Shoemaker-Levy 9 and Jupiter, K.S. Noll, H.A. Weaver, & P.D. Feldman, Eds. 183–212. Cambridge University Press.

53. ADUSHKIN, V.V. & I.V. NEMCHNOV. 1994. Consequences of impacts of cosmic bodies on the surface of the Earth. *In* Hazards Due to Comets and Asteroids, T. Gehrels, Ed.: 721–778. Univ. Arizona Press. Tucson, Arizona.

54. BEN-MENAHEM, A. 1975. Source parameters of the Siberian explosion of June 30, 1908, from analysis and synthesis of signals at four stations. Phys. Earth Planet. Inter. **11:** 1–35.

55. BJORAKER, G.L., S.R. STOLOVY, T.L. HERTER, G.E. GULL, & B.E. PIRGER. 1996. Detection of water after the collision of Fragment-G and Fragment-K of comet Shoemaker-Levy 9 with Jupiter. Icarus. **121:** 411–421.

56. CHYBA, C.F., P.J. THOMAS, & K.J. ZAHNLE. 1993. The 1908 Tunguska explosion: Atmospheric disruption of a stony asteriod. Nature. **361:** 40–44.

57. CLARKE, J.T., R. PRANG, G.E. BALLESTER, ET AL. 1995. HST far-ultraviolet imaging of Jupiter during the impacts of comet Shoemaker-Levy 9. Science. **267:** 1302–1307.

58. CRAWFORD, D.A. 1997. Comet Shoemaker-Levy 9 fragment size estimates: How big was the parent body? *In* Near-Earth Objects: The United Nations Conference on Near-Earth Objects, New York, April 24–26, 1995. Annals of the New York Academy of Sciences. This *volume*, **822:** 155–173.

59. FESENKOV, V.G. 1962. On the cometary nature of the Tunguska meteorite. Sov. Astron. English Translation. **5:** 441–451.
60. FLORENSKIY, K.P. 1963. Preliminary results from the 1961 combined Tunguska meteorite expedition. Meteoritica. **XXIII:** 3–37.
61. FORTOV, V.E., YU.N. GNEDIN, M.F. IVANOV. A.V. IVLEV, & B.A. KLUMOV. 1966. Collision of comet Shoemaker-Levy 9 with Jupiter: What did we see? Physics Uspekhi. **39:** 363–392.
62. GLASSTONE, S., ED. 1977. The Effects of Nuclear Weapons. U.S. Department of Defense/Department of Energy, Washington, D.C. 653 pp.
63. HAMMEL, H.B. 1996. HST imaging of Jupiter shortly after each impact: Plumes and fresh sites. *In* The Collision of Comet Shoemaker-Levy 9 and Jupiter, K.S. Noll, H.A. Weaver, & P.D. Feldman, Eds.: 111–120. Cambridge University Press.
64. HAMILTON, D.P., T.M. HERBST, A. RICHICHI, H. BÖHNHARDT, & J.L. ORTIZ. 1995. Calar Alto Observations of Shoemaker-Levy 9: Characteristics of the H and L Impacts. Geophys. Res. Lett. **22:** 2417.
65. HUNT, J.N., R. PALMER, & W. PENNEY. 1960. Atmospheric waves caused by large explosions. Philos. J.R. Soc. London. Sec. A. **252:** 275–315.
66. INGERSOLL, A. & H. KANAMORI. 1995. Waves from the impacts of Shoemaker-Levy 9 with Jupiter. Nature. **374:** 706–708.
67. KOROBEINICOV, V.P., P.I. CHUSHKIN, & L.V. SHURSHALOV. 1976. Mathematical model and computation of the Tunguska meteorite explosion. Acta Astronautica. **3:** 615–622.
68. KRINOV, E.L. 1963. The Tunguska and Sikhote-Alin meteorites. In the Moon, Meteorites, and Comets, B.M. Middlehurst & G,P, Kuiper, Eds.: 208–234. University of Chicago. Chicago, IL.
69. LAGAGE, P.O., P. GALDEMARD, E. PANTIN, ET AL. 1995. Collision of Shoemaker-Levy 9 fragments A, E, H, L, and Q1 with Jupiter: Mid-infrared light curves. Geophys. Res. Lett. **22:** 1773–1776.
70. MCGREGOR, P.J., P.D. NICHOLSON, & M.G. ALLEN. 1995. CASPIR observations of comet Shoemaker-Levy-9 with Jupiter. **121:** 361–388.
71. NORTON, O.R. 1997. Something is wrong at Sikhote-Alin, a mystery. Meteorite! **3:** (2) 34–35.
72. PRANGÉ, R., I.M. ENGLE, J.T. CLARKE, ET AL. 1995. Auroral signature of comet Shoemaker-Levy 9 in the Jovian atmosphere. Science. **267:** 1317–1320.
73. SEKANINA, Z. 1983. The Tunguska event: No cometary signature in evidence. The Astronomical Journal. **88:** 1382–1414.
74. SVETTSOV, V.V. 1995. A comet fall into the Jovian atmosphere. Solar System Research. **29:** 287–294.
75. TURCO, R.P., O.B. TOON, C. PARK, R.C. WHITTEN, J.B. POLLACK, & P. NOERDLINGER. 1982. An analysis of the physical, chemical, optical, and historical impacts of the 1908 Tunguska meteor fall. Icarus. **50:** 1–52.
76. YELLE, R.V. & M.A. MCGRATH. 1996. Ultraviolet spectroscopy of the SL9 impact sites. 1. The 175–230 nm region. Icarus. **119:** 90–11.
77. ZOLOTOV, A.B. 1967. Estimation of parameters of the Tungus meteorite based on new data. Sov. Phys. Dokl., English Translation. **11:** 108–111.
78. ZOTKIN, I.T. & M.A. TSIKULIN. 1966. Simulation of the explosion of the Tungus meteorite. Sov. Phys. Dokl., English Translation. **11:** 183–186.
79. Meadows, V. & D. Crisp. 1995. Impact plume composition from near-infrared spectroscopy. *In* Proceedings of the European SL-9/Jupiter workshop, R. West & H. Bonhardt, Eds.: 239.
80. Reed, J.W. 1987. Air-pressure waves from Mount St. Helens eruptions. J. Geophysical. Res. **92:** 11979–11992.